

12-2022

## Atomic Force Microscopy Cantilever-Based Nanoindentation: Mechanical Property Measurements at the Nanoscale in Air and Fluid

Ashton E. Enriques  
*Boise State University*

Sean Howard  
*Boise State University*

Raju Timsina  
*Boise State University*

Nawal K. Khadka  
*Boise State University*

Amber N. Hoover  
*Idaho National Laboratory*

*See next page for additional authors*

---

### Publication Information

Enriques, Ashton E.; Howard, Sean; Timsina, Raju; Khadka, Nawal K.; Hoover, Amber N.; Ray, Allison E.; . . . and Davis, Paul H. (2022). "Atomic Force Microscopy Cantilever-Based Nanoindentation: Mechanical Property Measurements at the Nanoscale in Air and Fluid". *Journal of Visualized Experiments*, 190, e64497. <https://doi.org/10.3791/64497>

This is a post-reviewed, pre-publication proof version of this article. The final, definitive version of this document will be published online at *Journal of Visualized Experiments*, published by MyJove Corporation. Copyright restrictions may apply. <https://doi.org/10.3791/64497>

---

**Authors**

Ashton E. Enriques, Sean Howard, Raju Timsina, Nawal K. Khadka, Amber N. Hoover, Allison E. Ray, Ling Ding, Chioma Onwumelu, Stephan Nordeng, Laxman Mainali, Gunes Uzer, and Paul H. Davis

# Atomic Force Microscopy Cantilever-Based Nanoindentation: Mechanical Property Measurements at the Nanoscale in Air and Fluid

Ashton E. Enriques<sup>1</sup>, Sean Howard<sup>2</sup>, Raju Timsina<sup>3</sup>, Nawal K. Khadka<sup>3</sup>, Amber N. Hoover<sup>4</sup>, Allison E. Ray<sup>5</sup>, Ling Ding<sup>4</sup>, Chioma Onwumelu<sup>6</sup>, Stephan Nordeng<sup>6</sup>, Laxman Mainali<sup>3,7</sup>, Gunes Uzer<sup>2</sup>, Paul H. Davis<sup>1,8</sup>

<sup>1</sup> Micron School of Materials Science & Engineering, Boise State University <sup>2</sup> Department of Mechanical & Biomedical Engineering, Boise State University <sup>3</sup> Department of Physics, Boise State University <sup>4</sup> Energy and Environmental Science and Technology, Idaho National Laboratory <sup>5</sup> Science and Technology, Idaho National Laboratory <sup>6</sup> Harold Hamm School of Geology & Geological Engineering, University of North Dakota <sup>7</sup> Biomolecular Sciences Graduate Program, Boise State University <sup>8</sup> Center for Advanced Energy Studies

## Corresponding Author

Paul H. Davis  
[pauldavis2@boisestate.edu](mailto:pauldavis2@boisestate.edu)

## Citation

Enriques, A.E., Howard, S., Timsina, R., Khadka, N.K., Hoover, A.N., Ray, A.E., Ding, L., Onwumelu, C., Nordeng, S., Mainali, L., Uzer, G., Davis, P.H. Atomic Force Microscopy Cantilever-Based Nanoindentation: Mechanical Property Measurements at the Nanoscale in Air and Fluid. *J. Vis. Exp.* (), e64497, doi:10.3791/64497 (2022).

## Date Published

November 29, 2022

## DOI

10.3791/64497

## URL

[jove.com/t/64497](https://jove.com/t/64497)

## Abstract

An atomic force microscope (AFM) fundamentally measures the interaction between a nanoscale AFM probe tip and the sample surface. If the force applied by the probe tip and its contact area with the sample can be quantified, it is possible to determine the nanoscale mechanical properties (e.g., elastic or Young's modulus) of the surface being probed. A detailed procedure for performing quantitative AFM cantilever-based nanoindentation experiments is provided here, with representative examples of how the technique can be applied to determine the elastic moduli of a wide variety of sample types, ranging from kPa to GPa. These include live mesenchymal stem cells (MSCs) and nuclei in physiological buffer, resin-embedded dehydrated loblolly pine cross-sections, and Bakken shales of varying composition.

Additionally, AFM cantilever-based nanoindentation is used to probe the rupture strength (i.e., breakthrough force) of phospholipid bilayers. Important practical considerations such as method choice and development, probe selection and calibration, region of interest identification, sample heterogeneity, feature size and aspect ratio, tip wear, surface roughness, and data analysis and measurement statistics are discussed to aid proper implementation of the technique. Finally, co-localization of AFM-derived nanomechanical maps with electron microscopy techniques that provide additional information regarding elemental composition is demonstrated.

## Introduction

Understanding the mechanical properties of materials is one of the most fundamental and essential tasks in engineering. For the analysis of bulk material properties, there are numerous methods available to characterize the mechanical properties of material systems, including tensile tests<sup>1</sup>, compression tests<sup>2</sup>, and three- or four-point bending (flexural) tests<sup>3</sup>. While these microscale tests can provide invaluable information regarding bulk material properties, they are generally conducted to failure, and are hence destructive. Additionally, they lack the spatial resolution necessary to accurately investigate the micro- and nanoscale properties of many material systems that are of interest today, such as thin films, biological materials, and nanocomposites. To begin addressing some of the problems with large-scale mechanical testing, mainly its destructive nature, microhardness tests were adopted from mineralogy. Hardness is a measure of the resistance of a material to plastic deformation under specific conditions. In general, microhardness tests use a stiff probe, usually made from hardened steel or diamond, to indent into a material. The resulting indentation depth and/or area can then be used to determine the hardness. Several methods have been developed, including Vickers<sup>4</sup>, Knoop<sup>5</sup>, and Brinell<sup>6</sup> hardness; each provides a measure of microscale material hardness, but under different conditions and definitions, and

as such only produces data that can be compared to tests performed under the same conditions.

Instrumented nanoindentation was developed to improve upon the relative values obtained *via* the various microhardness testing methods, improve the spatial resolution possible for the analysis of mechanical properties, and enable the analysis of thin films. Importantly, by utilizing the method first developed by Oliver and Pharr<sup>7</sup>, the elastic or Young's modulus,  $E$ , of a sample material can be determined *via* instrumented nanoindentation. Furthermore, by employing a Berkovich three-sided pyramidal nanoindenter probe (whose ideal tip area function matches that of the Vickers four-sided pyramidal probe)<sup>8</sup>, direct comparison between nanoscale and more traditional microscale hardness measurements can be made. With the growth in popularity of the AFM, AFM cantilever-based nanoindentation began receiving attention as well, particularly for measuring the mechanical properties of softer materials. As a result, as depicted schematically in **Figure 1**, the two most commonly employed techniques today to interrogate and quantify nanoscale mechanical properties are instrumented nanoindentation (**Figure 1A**) and AFM cantilever-based nanoindentation (**Figure 1B**)<sup>9</sup>, the latter of which is the focus of this work.

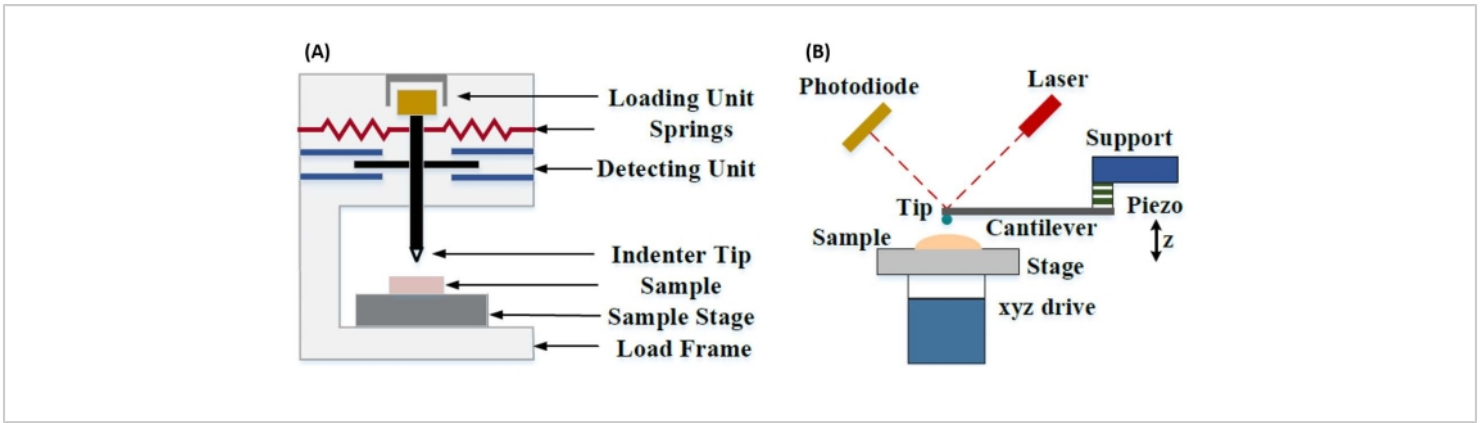


**Figure 1: Comparison of instrumented and AFM cantilever-based nanoindentation systems.** Schematic diagrams depicting typical systems for conducting (A) instrumented nanoindentation and (B) AFM cantilever-based nanoindentation. This figure was modified from Qian et al.<sup>51</sup>. Abbreviation: AFM = atomic force microscopy. [Please click here to view a larger version of this figure.](#)

Both instrumented and AFM cantilever-based nanoindentation employ a stiff probe to deform a sample surface of interest and monitor the resultant force and displacement as a function of time. Typically, either the desired load (i.e., force) or (Z-piezo) displacement profile is specified by the user *via* the software interface and directly controlled by the instrument, while the other parameter is measured. The mechanical property most often obtained from nanoindentation experiments is the elastic modulus ( $E$ ), also referred to as the Young's modulus, which has units of pressure. The elastic modulus of a material is a fundamental property relating to the bond stiffness and is defined as the ratio of tensile or compressive stress ( $\sigma$ , the applied force per unit area) to axial strain ( $\epsilon$ , the proportional deformation along the indentation axis) during elastic (i.e., reversible or temporary) deformation prior to the onset of plastic deformation (equation [1]):

$$E = \frac{\sigma}{\epsilon} \quad (1)$$

It should be noted that, because many materials (especially biological tissues) are in fact viscoelastic, in reality, the (dynamic or complex) modulus consists of both elastic (storage, in phase) and viscous (loss, out of phase) components. In actual practice, what is measured in a nanoindentation experiment is the reduced modulus,  $E^*$ , which is related to the true sample modulus of interest,  $E$ , as shown in equation (2):

$$\frac{1}{E^*} = \frac{1-\nu^2}{E} + \frac{1-\nu_{tip}^2}{E_{tip}} \quad (2)$$

Where  $E_{tip}$  and  $\nu_{tip}$  are the elastic modulus and Poisson's ratio, respectively, of the nanoindenter tip, and  $\nu$  is the estimated Poisson's ratio of the sample. The Poisson's ratio is the negative ratio of the transverse to axial strain, and hence indicates the degree of transverse elongation of a sample upon being subjected to axial strain (e.g., during nanoindentation loading), as shown in equation (3):

$$\nu = -\frac{d\epsilon_{trans}}{d\epsilon_{axial}} \quad (3)$$

The conversion from reduced to actual modulus is necessary because a) some of the axial strain imparted by the indenter tip may be converted to transverse strain (i.e., the sample may deform *via* expansion or contraction perpendicular to the direction of loading), and b) the indenter tip is not infinitely hard, and thus the act of indenting the sample results in some (small) amount of deformation of the tip. Note that in the case where  $E_{tip} \gg E$  (i.e., the indenter tip is much harder than the sample, which is often true when using a diamond probe), the relationship between the reduced and actual sample modulus simplifies greatly to  $E \approx E^*(1 - \nu^2)$ . While instrumented nanoindentation is superior in terms of accurate force characterization and dynamic range, AFM cantilever-based nanoindentation is faster, provides orders of magnitude greater force and displacement sensitivity, enables higher resolution imaging and improved indentation locating, and can simultaneously probe nanoscale magnetic and electrical properties<sup>9</sup>. In particular, AFM cantilever-based nanoindentation is superior for the quantification of mechanical properties at the nanoscale of soft materials (e.g., polymers, gels, lipid bilayers, and cells or other biological materials), extremely thin (sub- $\mu\text{m}$ ) films (where substrate effects can come into play depending upon indentation depth)<sup>10,11</sup>, and suspended two-dimensional (2D) materials<sup>12,13,14</sup> such as graphene<sup>15,16</sup>, mica<sup>17</sup>, hexagonal boron nitride (h-BN)<sup>18</sup>, or transition metal dichalcogenides (TMDCs; e.g., MoS<sub>2</sub>)<sup>19</sup>. This is due to its exquisite force (sub-nN) and displacement (sub-nm) sensitivity, which is important for accurately determining the initial point of contact and remaining within the elastic deformation region.

In AFM cantilever-based nanoindentation, displacement of an AFM probe toward the sample surface is actuated by a calibrated piezoelectric element (**Figure 1B**), with the

flexible cantilever eventually bending due to the resistive force experienced upon contact with the sample surface. This bending or deflection of the cantilever is typically monitored by reflecting a laser off the back of the cantilever and into a photodetector (position sensitive detector [PSD]). Coupled with the knowledge of the cantilever stiffness (in nN/nm) and deflection sensitivity (in nm/V), it is possible to convert this measured cantilever deflection (in V) into the force (in nN) applied to the sample. Following contact, the difference between the Z-piezo movement and the cantilever deflection yields the sample indentation depth. Combined with the knowledge of the tip area function, this enables calculation of the tip-sample contact area. The slope of the in-contact portions of the resulting force-distance or force-displacement (F-D) curves can then be fit using an appropriate contact mechanics model (see the **Data Analysis** section of the discussion) to determine the nanomechanical properties of the sample. While AFM cantilever-based nanoindentation possesses some distinct advantages over instrumented nanoindentation as described above, it also presents several practical implementation challenges, such as calibration, tip wear, and data analysis, which will be discussed here. Another potential downside of AFM cantilever-based nanoindentation is the assumption of linear elasticity, as the contact radius and indentation depths need to be much smaller than the indenter radius, which can be difficult to achieve when working with nanoscale AFM probes and/or samples exhibiting significant surface roughness.

Traditionally, nanoindentation has been limited to individual locations or small grid indentation experiments, wherein a desired location (i.e., region of interest [ROI]) is selected and a single controlled indent, multiple indents in a single location separated by some waiting time, and/or a coarse

grid of indents are performed at a rate on the order of Hz. However, recent advances in AFM allow for the simultaneous acquisition of mechanical properties and topography through the utilization of high-speed force curve-based imaging modes (referred to by various tradenames depending on the system manufacturer), wherein force curves are conducted at a kHz rate under load control, with the maximum tip-sample force utilized as the imaging setpoint. Point-and-shoot methods have also been developed, allowing for the acquisition of an AFM topography image followed by subsequent selective nanoindentation at points of interest within the image, affording nanoscale spatial control over nanoindentation location. While not the primary focus of this work, specific selected **application examples** of both force curve-based imaging and point-and-shoot cantilever-based nanoindentation are presented in the representative results, and can be used in conjunction with the protocol outlined below if available on the particular AFM platform employed. Specifically, this work outlines a generalized protocol for the practical implementation of AFM cantilever-based nanoindentation on any capable AFM system and provides four use case examples (two in air, two in fluid) of the technique, including representative results and an in-depth discussion of the nuances, challenges, and important considerations to successfully employ the technique.

## Protocol

**NOTE:** Due to the wide variety of commercially available AFMs and diversity of sample types and applications that exist for cantilever-based nanoindentation, the protocol that follows is intentionally designed to be relatively general in nature, focusing on the shared steps necessary for all cantilever-based nanoindentation experiments regardless of instrument or manufacturer. Because of this, the authors assume the

reader possesses at least basic familiarity with operating the specific instrument chosen for performing cantilever-based nanoindentation. However, in addition to the general protocol outlined below, a detailed step-by-step standard operating procedure (SOP) specific to the AFM and software used here (see **Table of Materials**), focused on cantilever-based nanoindentation of samples in fluid, is included as a **Supplementary Material**.

### 1. Sample preparation and instrument setup

1. Prepare the sample in a manner that minimizes both surface roughness (ideally nanometer-scale, ~10x less than the intended indentation depth) and contamination without altering the mechanical properties of the area(s) of interest.
2. Select an appropriate AFM probe for nanoindentation of the intended sample based on the medium (i.e., air or fluid), expected modulus, sample topography, and relevant feature sizes (see the **probe selection considerations** in the discussion). Load the probe onto the probe holder (see **Table of Materials**) and attach the probe holder to the AFM scan head.
3. Select an appropriate nanoindentation mode in the AFM software that affords user control of individual ramps (i.e., force-displacement curves).
4. Align the laser onto the back of the probe cantilever, opposite the location of the probe tip and into the PSD.

**NOTE:** The specific mode will differ across different AFM manufacturers and individual instruments (see SOP provided in the **Supplementary Material** for more details and a specific example).

**NOTE:** See the mesenchymal stem cell **application example** for more details regarding important

considerations when aligning the laser and conducting nanoindentation in fluid, in particular, avoiding floating debris and/or air bubbles, which can scatter or refract the beam. The AFM optics may also need to be adjusted to compensate for the index of refraction of the fluid and to avoid crashing the probe when engaging the surface.

1. Center the laser beam spot on the back of the cantilever by maximizing the sum voltage (**Figure 2A**).
2. Center the reflected laser beam spot on the PSD by adjusting the X and Y (i.e., horizontal and

vertical) deflection signals to be as close to zero as possible (**Figure 2A**), thereby providing the maximum detectable deflection range for producing an output voltage proportional to the cantilever deflection.

5. If unsure of the sample topography, surface roughness, and/or surface density (in the case of flakes or particles), perform an AFM topography survey scan prior to any nanoindentation experiments to confirm sample suitability, as described in step 1.1 and the sample preparation portion of the discussion.

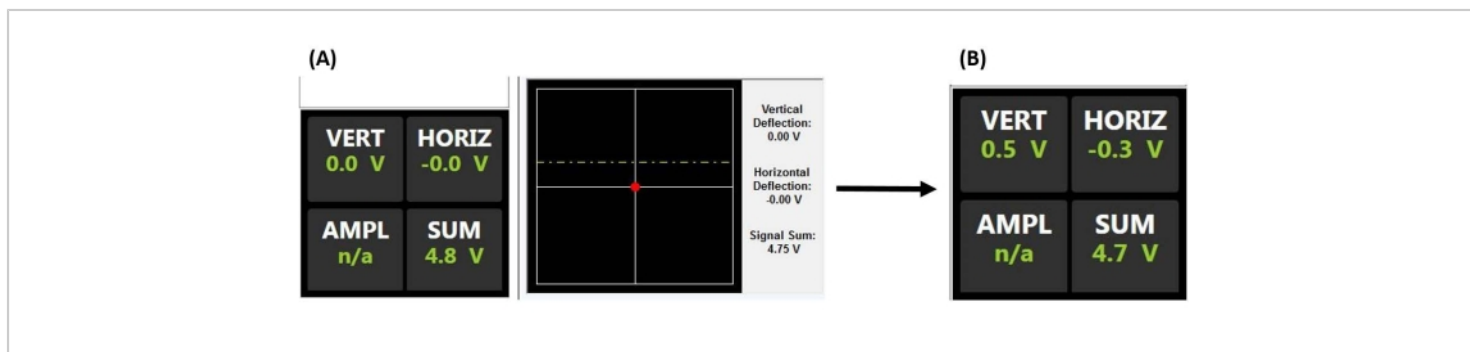


**Figure 2: Position-sensitive detector monitor.** (A) PSD display indicating a properly aligned laser reflecting off the back of the probe cantilever and onto the center of the PSD (as evidenced by the large sum voltage and lack of vertical or horizontal deflection) prior to engaging on the sample surface (i.e., probe out of contact with the sample). (B) The vertical deflection voltage increases when the cantilever is deflected (e.g., when the probe makes contact with the sample). Abbreviations: PSD = position-sensitive detector; VERT = vertical; HORIZ = horizontal; AMPL = amplitude; n/a = not applicable. [Please click here to view a larger version of this figure.](#)

## 2. Probe calibration

**NOTE:** Three values are necessary to quantify the mechanical properties of a sample using the F-D curve data collected during cantilever-based nanoindentation: the **deflection sensitivity (DS) of the cantilever/PSD system** (nm/V or V/nm), the **cantilever spring constant** (nN/nm), and the **probe contact area**, often expressed in terms of the

effective probe tip radius (nm) at a given indentation depth less than the probe radius in the case of a spherical probe tip.

1. Calibrate the DS of the probe/AFM system by ramping on an extremely hard material (e.g., sapphire,  $E = 345$  GPa) so that deformation of the sample is minimized and thus the measured Z movement of the piezo following



the initiation of tip-sample contact is converted solely into cantilever deflection.

**NOTE:** The DS calibration must be performed under the same conditions as the planned nanoindentation experiments (i.e., temperature, medium, etc.) to accurately reflect the DS of the system during the experiments. A long (30 min) laser warmup period may be necessary for maximum accuracy to allow time for thermal equilibrium to be reached and stable laser output power and pointing stability to be established. The DS must be remeasured **every** time the laser is realigned, even if the same probe is used, as the DS depends on the laser intensity and position on the cantilever, as well as the quality of the reflection from the probe (i.e., degradation of the probe's backside coating will affect the DS) and sensitivity of the PSD<sup>20</sup>.

1. Set up and perform the **DS calibration indents** on the sapphire to achieve approximately the same probe deflection (in V or nm) as the planned sample indents, since the measured displacement is a function of the tip deflection angle and becomes nonlinear for large deflections.
2. Determine the **DS** (in nm/V), or alternatively, the inverse optical lever sensitivity (in V/nm), from the slope of the linear portion of the in-contact regime after the initial contact point in the resulting F-D curve, as shown in **Figure 3A**.
3. Repeat the ramp at least 5x, recording each DS value. Use the average of the values for maximum accuracy. If the relative standard deviation (RSD) of the measurements exceeds ~1%, remeasure the DS, as sometimes the first few F-D curves are nonideal due to the initial introduction of adhesive forces.

4. If the probe cantilever's **spring constant**,  $k$ , is not factory-calibrated (e.g., *via* laser Doppler vibrometry [LDV]), calibrate the spring constant.

**NOTE:** The thermal tune method is optimal for relatively soft cantilevers with  $k < 10$  N/m (see the **spring constant** section of the discussion for a list and description of alternative methods, particularly for stiff cantilevers with  $k > 10$  N/m). As shown in **Figure 3B, C**, thermal tuning is typically integrated into the AFM control software.

2. If the probe does not come with a factory-calibrated tip radius measurement (e.g., *via* scanning electron microscope [SEM] imaging), measure the effective tip radius,  $R$ .

**NOTE:** There are two common methods for measuring the **tip radius** (see corresponding discussion section), but the most common for nanometer-scale probe tips is the blind tip reconstruction (BTR) method, which utilizes a roughness standard (see **Table of Materials**) containing numerous extremely sharp (sub-nm) features that serve to effectively image the tip, rather than the tip imaging the sample.

1. If employing the BTR method, image the roughness (tip characterization) sample using a slow scan rate (<0.5 Hz) and high feedback gains to help optimize tracking of the very sharp features. Choose an image size and pixel density (resolution) based on the expected tip radius (e.g., a 1024 x 1024 pixel image of a 3  $\mu\text{m}$  x 3  $\mu\text{m}$  area will have ~3 nm lateral resolution).
2. Use AFM image analysis software (see **Table of Materials**) to model the probe tip and estimate its

end radius and effective tip diameter at the expected sample indentation depth, as shown in **Figure 3D-F**.

3. Upon completing the probe calibration, enter the DS,  $k$ , and  $R$  values in the instrument software, as shown in **Figure 4A**.

1. Enter an estimate of the sample's Poisson's ratio,  $\nu$ , to enable converting the measured reduced modulus to the actual sample modulus<sup>9</sup>.

If employing a conical or conispherical contact mechanics model based on the tip shape and indentation depth, it is also necessary to enter the tip half angle (**Figure 4C**).

**NOTE:** The modulus is relatively insensitive to small errors or uncertainties in the estimated Poisson's ratio. An estimate of  $\nu = 0.2-0.3$  is a good starting point for many materials<sup>21</sup>.

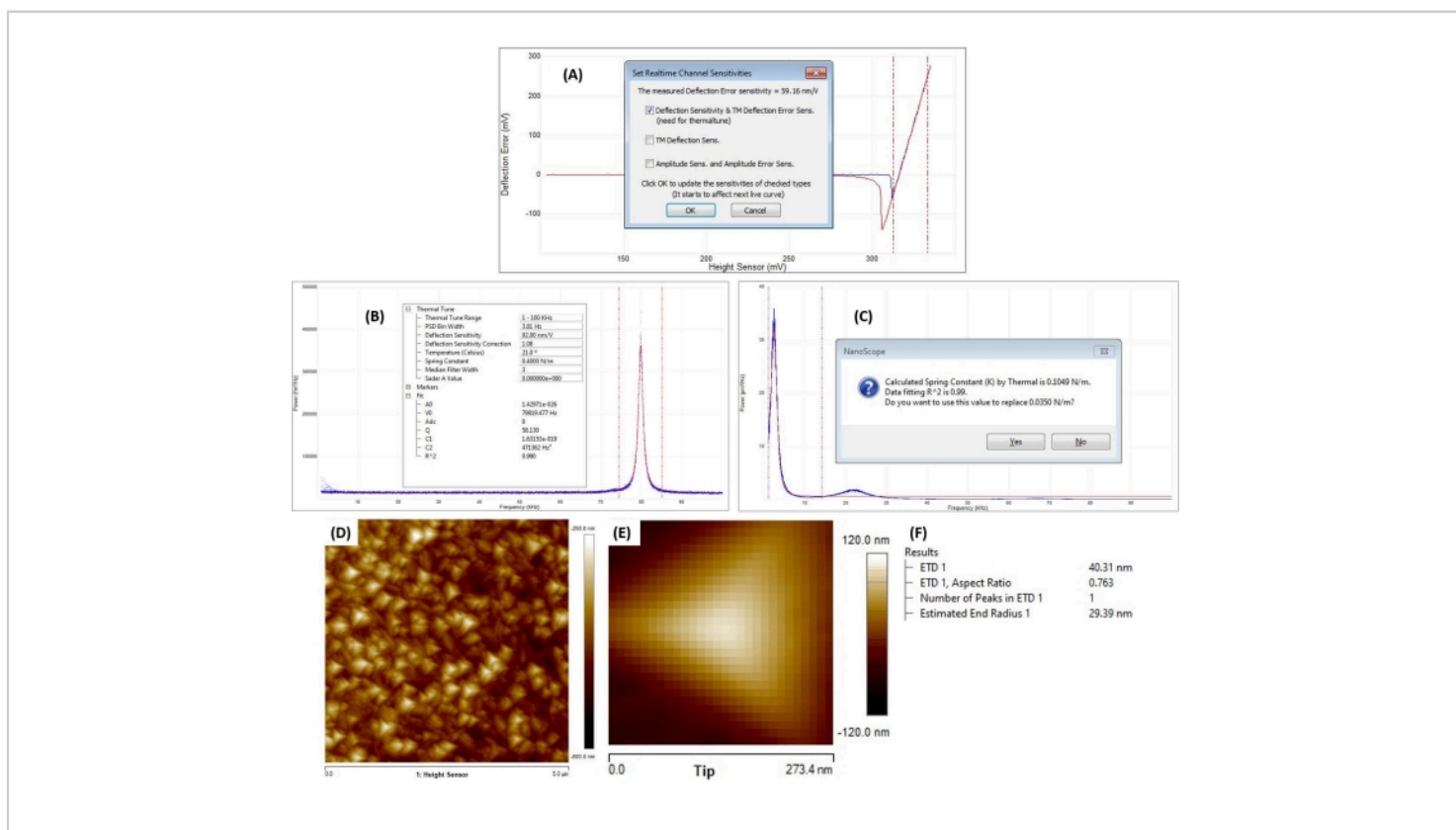


**Figure 3: Probe calibration.** (A) Deflection sensitivity determination. Result of a representative deflection sensitivity measurement carried out on a sapphire substrate ( $E = 345$  GPa) for a standard tapping mode probe (nominal  $k = 42$  N/m; see **Table of Materials**) with a reflective backside aluminum coating. Shown are the measured approach (blue trace) and retract or withdraw (red trace) curves. The measured deflection sensitivity of 59.16 nm/V was determined by fitting the approach curve between the snap-to-contact and turn-around points, as indicated by the region between the vertical dotted red lines. The region of negative-going deflection evident in the retract/withdraw curve prior to pulling off the surface is indicative of tip-sample adhesion. (B,C) Thermal tuning. Representative cantilever thermal noise spectra (blue traces) with corresponding fits (red traces) for two different probes. (B) Thermal tune setup and fit parameters for a standard

force curve-based AFM imaging probe (see **Table of Materials**) with its nominal spring constant  $k = 0.4$  N/m used as an initial guess. The fit of the cantilever thermal noise spectrum yields a fundamental resonance frequency of  $f_0 = 79.8$  kHz, which is in reasonably good agreement with the nominal value of  $f_0 = 70$  kHz. The measured Q factor is 58.1. Goodness of fit ( $R^2 = 0.99$ ) is based on agreement of the fit with the data between the two vertical dashed red lines. Note that it is important to know and enter both the ambient temperature and deflection sensitivity for accurate results. **(C)** Cantilever thermal noise spectrum and corresponding fit (i.e., thermal tune) with resultant calculated spring constant  $k = 0.105$  N/m for an extremely soft cantilever used for performing nanomechanical measurements on live cells and isolated nuclei. Note the significantly lower natural resonance frequency of  $\sim 2$ -3 kHz. **(D-F)** Blind tip reconstruction. Representative blind tip reconstruction workflow for a diamond tip probe (nominal  $R = 40$  nm; see **Table of Materials**). **(D)** A  $5 \mu\text{m} \times 5 \mu\text{m}$  image of a tip characterization sample consisting of a series of extremely sharp (sub-nm) titanium spikes that serve to image the AFM probe tip. **(E)** Resultant reconstructed model (inverted height image) of the probe tip. **(F)** Blind tip reconstruction fitting results, including an estimated end radius of  $R = 29$  nm and effective tip diameter of 40 nm at a user selected height of 8 nm (i.e., indentation depth  $\ll R$ ) from the tip apex, calculated by converting the tip-sample contact area at that height into an effective diameter assuming a circular profile (i.e.,  $A = \pi r^2 = \pi(d/2)^2$ ) for use with spherical contact mechanics models. Abbreviations: AFM = atomic force microscopy; ETD = effective tip diameter. [Please click here to view a larger version of this figure.](#)

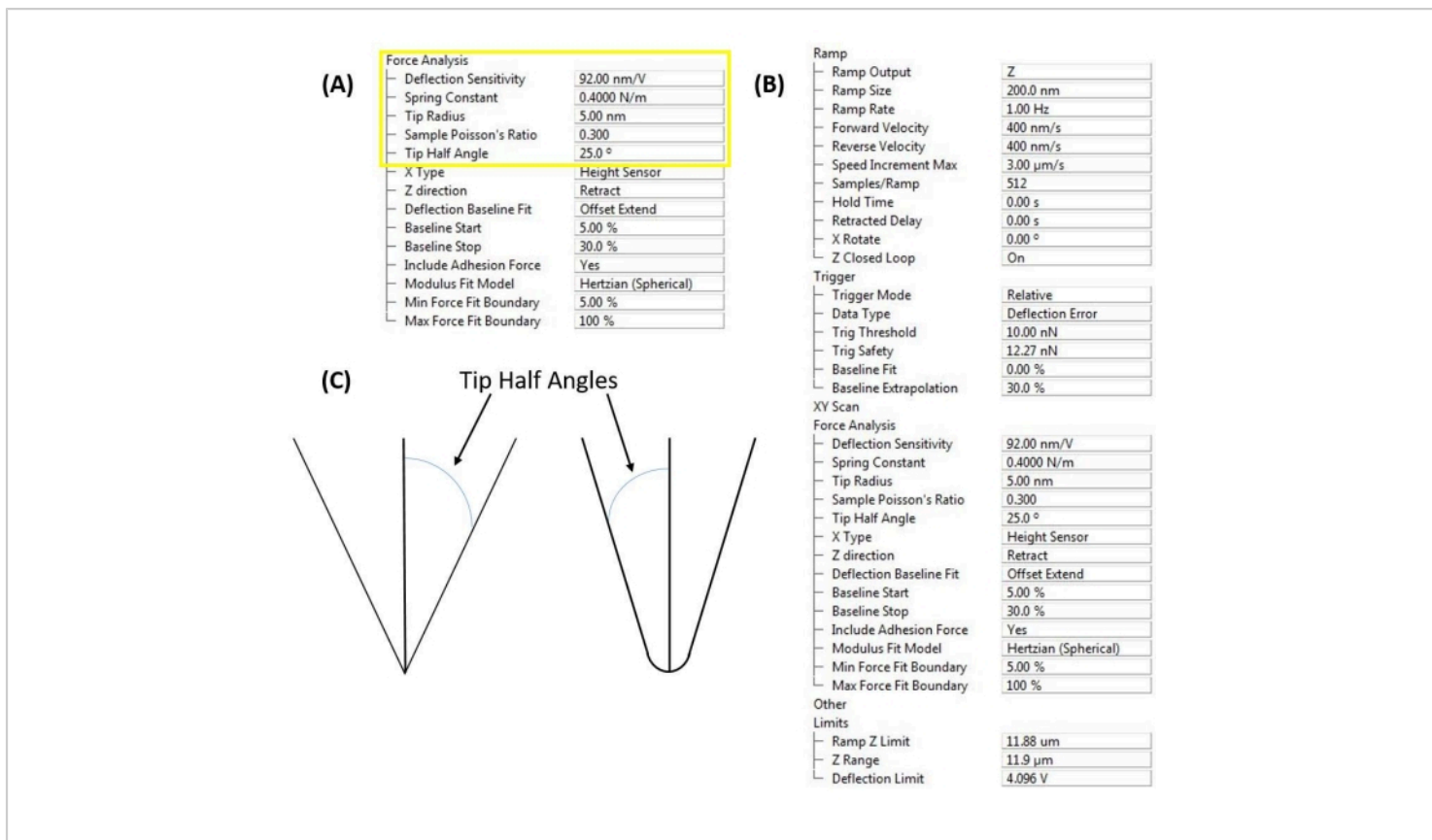


**Figure 4: Software interface inputs.** (A) Probe calibration constants. Software user interface (see **Table of Materials**) to enter measured deflection sensitivity, spring constant, and tip radius to enable quantitative nanomechanical measurements. The Poisson's ratio of both the probe and sample are necessary for calculating the elastic or Young's modulus of the sample from the cantilever-based nanoindentation force curves. (B) Ramp control window. Software user interface (see **Table of Materials**) for setting up cantilever-based nanoindentation experiments, organized into the parameters describing the ramp itself (i.e., indentation profile), instrument triggering (e.g., force vs. displacement control), subsequent force analysis, and movement limits (to improve measurement sensitivity by narrowing the range over which the A/D converter has to operate in controlling the Z-piezo and reading the PSD deflection). (C) The tip half angle (based on the probe geometry or direct measurement) is important if a conical, pyramidal, or conispherical contact mechanics model (e.g., Sneddon) is employed.

[Please click here to view a larger version of this figure.](#)

### 3. Collect force-displacement (F-D) data

**NOTE:** The parameter values presented here (see **Figure 4B**) may vary depending upon the force and indentation range for a given sample.

1. Navigate the sample under the AFM head and engage on the desired region of interest.
  1. Monitor the vertical deflection signal (**Figure 2B**) or perform a small (~50-200 nm) initial ramp (**Figure**

**4B)** to verify that the tip and sample are in contact (see **Figure 5A**).

2. Adjust the AFM head position slightly upward (in steps corresponding to ~50% of the full ramp size) and ramp again. Repeat until the tip and sample are just out of contact, as evidenced by a nearly flat ramp (**Figure 5B**) and minimal vertical deflection of the cantilever (**Figure 2A**).

3. Once no obvious tip-sample interaction is present (compare **Figure 2A** and **Figure 2B**), lower the AFM head by an amount corresponding to ~50%-100% of the ramp size to ensure the probe tip will not crash into the sample while manually moving the AFM head. Ramp again, repeating until either a good curve (**Figure 5D**) or a curve similar to **Figure 5C** is observed. In the latter case, perform one additional small AFM head-lowering adjustment equal to ~20%-50% of the ramp size to achieve good contact and a force curve similar to that shown in **Figure 5D**.

2. Adjust ramp parameters (as described below and shown in **Figure 4B**) to optimize for the instrument, probe, and sample, and obtain ramps similar to that shown in **Figure 5D**.

1. Select an appropriate ramp size (i.e., total Z-piezo movement through one ramp cycle) depending on the sample (e.g., thickness, expected modulus, surface roughness) and desired indentation depth.

**NOTE:** For stiffer samples, less sample deformation (and hence more probe deflection for a given Z-piezo movement) is likely to occur, so the ramp size can generally be smaller than for softer samples. Typical ramp sizes for stiff samples and cantilevers may be

tens of nm, while for soft samples and cantilevers ramps may be hundreds of nm to a few  $\mu\text{m}$  in size; specific selected **application examples** are presented in the representative results section. Note that minimum and maximum possible ramp sizes are instrument-dependent.

2. Select an appropriate ramp rate (1 Hz is a good starting point for most samples).

**NOTE:** The ramp rate may be limited by control and/or detection electronic speeds/bandwidths. In combination with the ramp size, the ramp rate determines the tip velocity. The tip velocity is particularly important to consider when indenting soft materials where viscoelastic effects may cause hysteresis artifacts<sup>9,22</sup>.

3. Choose whether to employ a triggered (load-controlled) or untriggered (displacement-controlled) ramp.

**NOTE:** In a triggered ramp, the system will approach the sample in user-defined steps (based on the ramp size and resolution or number of data points) until the desired trigger threshold (i.e., setpoint force or cantilever deflection) is detected, at which point the system will retract to its original position and display the F-D curve. In an untriggered ramp, the system simply extends the Z-piezo the distance specified by the user defined ramp size and displays the measured F-D curve. Triggered ramps are preferred for most use cases, but untriggered ramps can be useful when investigating soft materials that do not exhibit a sharp, easily identifiable contact point.

1. If a **triggered ramp** is chosen, set the **trigger threshold** (user-defined maximum allowed

force or deflection of the ramp) to result in the desired indentation into the sample.

**NOTE:** Use of a trigger threshold means that a ramp may terminate (i.e., the probe may begin to retract) before reaching the full ramp size (Z-piezo extension) specified. Values may range from a few nN to a few  $\mu\text{N}$ , depending on the tip-sample system.

2. Set the **ramp position** to determine the portion of the Z-piezo's maximum range that will be used to execute the ramp. Ensure that the **total range of the ramp size** does not start or end outside of the maximum Z-piezo range (see representative examples in **Figure 6**), otherwise a portion of the F-D curve will not represent any physical measurement (i.e., the Z-piezo will be fully extended or retracted, not moving).
4. Set the **number of samples/ramp** (e.g., 512 samples/ramp) to achieve the desired resolution of the measurement (i.e., point density of the F-D curve).

**NOTE:** The maximum samples/ramp may be limited by software (file size) or hardware constraints (e.g., analog to digital [A/D] conversion speed, depending upon the ramp rate). It is also possible to limit the allowable Z-piezo or deflection range (see limits parameters in **Figure 4B**) to increase the effective resolution of the system's A/D converter.

5. Set the **X-rotate** to reduce the shear forces on the sample and tip by simultaneously moving the probe slightly in the X-direction (parallel to the cantilever) while indenting in the Z-direction (perpendicular to cantilever). Use a value for the X-rotate equal to the offset angle of the probe holder relative to the surface normal ( $12^\circ$  is typical).

**NOTE:** The X-rotate is necessary because the cantilever is mounted in the probe holder at a small angle relative to the surface to allow the incident laser beam to reflect into the PSD. Additionally, the front and back angles of the probe tip may differ from each other (i.e., the probe tip may be asymmetrical). More specific information can be obtained from individual probe and AFM manufacturers.

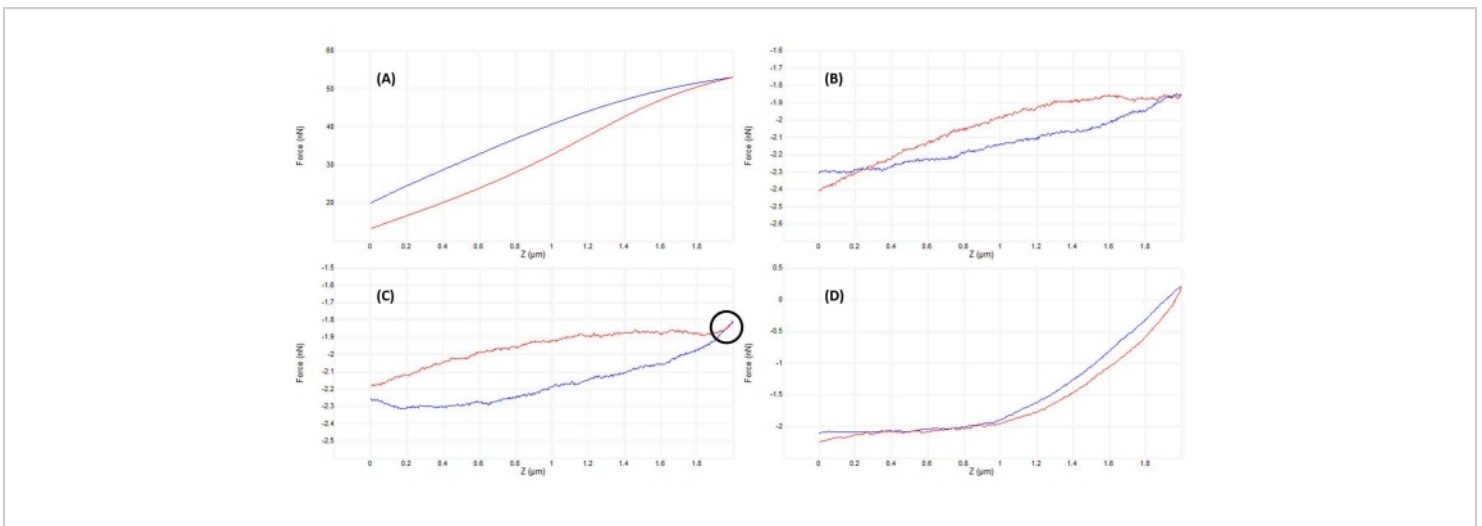


**Figure 5: Optimizing tip-sample separation after engaging to obtain good force curves.** Sequential examples of representative force-displacement curves obtained while indenting in fluid (phosphate-buffered saline) on a live mesenchymal stem cell nucleus with a calibrated soft silicon nitride cantilever (nominal  $k = 0.04$  N/m) terminating in a  $5\ \mu\text{m}$  radius hemispherical tip (see **Table of Materials**). Curves were obtained in the process of engaging the cell surface and optimizing the indentation parameters, with probe approach shown in blue and retract/withdraw in red. **(A)** The tip is already engaged and in contact with the sample prior to beginning the ramp, leading to large cantilever deflection and forces, with no flat precontact baseline. **(B)** After manually moving the tip sufficiently far away from the sample, an untriggered  $2\ \mu\text{m}$  ramp results in an F-D curve that is nearly flat (i.e., virtually no change in force). In ambient conditions, the curve would be flatter, but in fluid, the viscosity of the medium can cause slight deflections of the probe cantilever during a ramp as seen here, even with no surface contact. **(C)** After approaching slightly closer to the surface prior to beginning the ramp, the approach and retract curves show a slight increase in force (increased slope) near the turnaround point of the ramp (i.e., transition from approach to withdraw). The telltale sign to look for is that the approach (blue) and withdraw (red) curves begin to overlap (region indicated by the black circle), which is indicative of a physical interaction with the surface. **(D)** An ideal F-D curve acquired after optimization of the ramp parameters and approaching slightly ( $\sim 1\ \mu\text{m}$ ) closer to the cell surface than in **C** so that the probe spends approximately half the ramp in contact with the cell, enabling sufficient deformation to fit the contact portion of the approach curve and determine the elastic modulus. The relatively long, flat, low-noise baseline makes it easier for the fitting algorithm to determine the contact point. Abbreviation: F-D = force-displacement. [Please click here to view a larger version of this figure.](#)

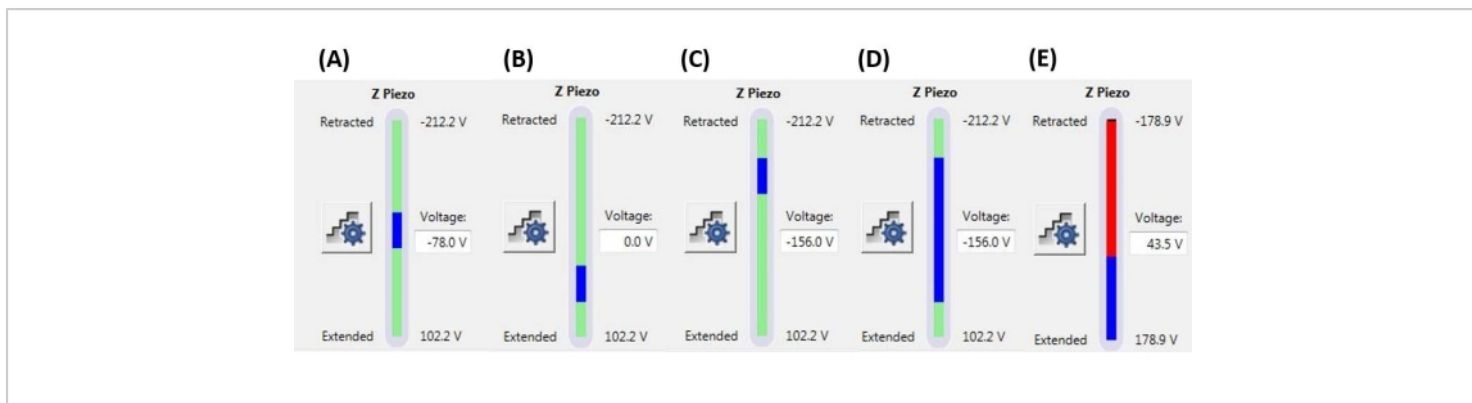


**Figure 6: Ramp size and position.** Z-piezo monitor showing the extent of the ramp (blue bar) relative to the total available Z-piezo movement range (green bar). **(A)** The Z-piezo position is near the middle of its range of movement, as indicated both by the blue bar being located roughly in the middle of the green bar and the current Z-piezo voltage (-78.0 V) being roughly between its fully retracted (-212.2 V) and extended (+102.2 V) values. **(B)** Z-piezo is extended relative to **A**, with no bias voltage applied. **(C)** Z-piezo is retracted relative to **A** and **B**. **(D)** The Z-piezo position is the same as in **C** at -156.0 V, but the ramp size has been increased relative to **A-C** to take advantage of more of the Z-piezo's full range of motion. **(E)** The ramp size is too large for the current ramp position, resulting in the Z-piezo being extended to the end of its range. This will cause the F-D curve to flatline as the system cannot extend the Z-piezo further. Abbreviation: F-D = force-displacement. [Please click here to view a larger version of this figure.](#)

#### 4. F-D curve analysis

1. Choose an appropriate data analysis software package.

Select and load the data to be analyzed.

**NOTE:** Many AFM manufacturers and AFM image processing software programs have built-in support for F-D curve analysis. Alternatively, the increased flexibility and features of a dedicated F-D curve analysis package, such as the open source AtomicJ software package, may be beneficial<sup>23</sup>, particularly for batch processing and statistical analysis of large datasets or implementing complex contact mechanics models.

2. Input calibrated values for the **spring constant**, **DS**, and **probe tip radius**, along with **estimates** of the **Young's modulus** and **Poisson's ratio** for the **probe tip** (based

on its material composition) and the **Poisson's ratio** of the sample.

**NOTE:** If using a diamond tip indenter, the values  $E_{tip} = 1140$  GPa and  $\nu_{tip} = 0.07$  can be used<sup>21,24,25,26</sup>. For a standard silicon probe,  $E_{tip} = 170$  GPa and  $\nu_{tip} = 0.27$  can typically be used, although the Young's modulus of silicon varies depending upon the crystallographic orientation<sup>27</sup>.

3. Choose a nanoindentation contact mechanics model appropriate for the tip and sample.

**NOTE:** For the many common spherical tip models (e.g., Hertz, Maugis, DMT, JKR), it is imperative that the indentation depth into the sample is less than the tip radius; otherwise the spherical geometry of the probe tip



gives way to a conical or pyramidal shape (**Figure 4C**).

For conical (e.g., Sneddon<sup>28</sup>) and pyramidal models, the tip half angle (i.e., the angle between the side wall of the tip and a bisecting line perpendicular to the tip end; **Figure 4C**) must be known and is usually available from the probe manufacturer. For more information regarding contact mechanics models, please see the **Data Analysis** section of the Discussion.

4. Run the fitting algorithm. Check for proper fitting of the F-D curves; a low residual error corresponding to an average  $R^2$  near unity (e.g.,  $R^2 > 0.9$ ) is typically indicative of a good fit to the chosen model<sup>29,30</sup>. Spot check individual curves to visually inspect the curve, model fit, and calculated contact points if desired (e.g., see **Figure 7** and the **Data Analysis** section of the discussion).

## Representative Results

### Force-displacement curves

**Figure 7** shows representative, near-ideal F-D curves obtained from nanoindentation experiments performed in air on resin-embedded loblolly pine samples (**Figure 7A**) and in fluid (phosphate-buffered saline [PBS]) on mesenchymal stem cell (MSC) nuclei (**Figure 7B**). The use of any contact mechanics model relies on the accurate and reliable determination of the initial tip-sample contact point. Thus, the relatively flat, low-noise baseline preceding the initial contact point and the smooth slope of the contact portion of the F-D curves shown in **Figure 7** makes them ideal for analysis to extract mechanical properties, as evidenced by the excellent agreement between the approach curves (blue traces) and corresponding fits (green traces) in the insets.

Conversely, there are several common issues that a user may encounter while performing cantilever-based nanoindentation that will lead to nonideal F-D curves. One of the most common issues, particularly immediately after engaging, is the probe tip already being in contact with the sample prior to initiation of a ramp (**Figure 5A**), which prevents the acquisition of the necessary out-of-contact baseline for determining the initial contact point. This can also lead to excessively large forces in the case of untriggered (i.e., controlled displacement) ramps. This is of particular concern when performing a large ramp with a stiff cantilever, as the resulting forces may break the cantilever and/or damage the sample or tip. To avoid this, monitor the vertical deflection voltage during and after the initial engage. If the measured vertical deflection voltage is positive (assuming proper initial alignment) as shown in **Figure 2B**, then the cantilever is being deflected and the tip is in contact with the sample. Larger positive voltages correspond to larger cantilever deflections, but regardless of the magnitude of the deflection, the user should manually raise the AFM head (e.g., by employing a stepper motor) away from the sample. The vertical deflection voltage should slowly decrease and may even temporarily dip below zero in the case of strong tip-sample adhesive forces, but will eventually reach 0 V (or close to 0 V) once the tip is no longer in contact with the sample (**Figure 2A**). From this point, the user can resume optimizing the ramp parameters and performing indents.

Another common problem (particularly for untriggered ramps) is for the entire F-D curve to appear nearly flat, with no obvious sign of tip-sample interaction, as shown previously in **Figure 5B**. If available on the instrument, the solution to this is to manually lower the SPM head by ~10% less than the ramp size (to avoid crashing the probe tip) and ramp again, repeating until an obvious increase in force is observed due

to tip-sample interaction (**Figure 5C,D**) before proceeding to optimize other ramp parameters.

### Tip wear

**Figure 8** presents an example of tip wear in an experimental setting. A single, stiff, silicon tapping mode AFM probe (see **Table of Materials**) was used to image several large areas of a Bakken shale sample (see corresponding **application example** for more details) using a rapid (kHz rate) force curve-based imaging method, and the BTR method was used to model the tip geometry and estimate the tip end radius before and after each of three consecutive images. The shale samples under investigation consisted of a matrix of clay and organic material ( $E \sim 5$  GPa) with much harder inorganic mineral inclusions dispersed throughout ( $E > 30$  GPa). Because the sample contained significant variations in surface topography ( $\pm 2 \mu\text{m}$ ) across the large scan areas ( $85 \mu\text{m} \times 85 \mu\text{m}$ ) imaged, the scan rate was set to the minimum allowable on the instrument used, 0.1 Hz. With a force curve acquisition rate of 2 kHz and a scan rate of 0.1 Hz, over the course of a single  $1024 \times 1024$  pixel image there were over 20 million tip-sample interactions. As a result, the probe tip experienced significant wear relative to its pristine state (**Figure 8A**) over the course of imaging the sample, increasing by over an order of magnitude from an effective end radius of  $\sim 11$  nm as received to  $\sim 129$  nm at the conclusion of the three images (**Figure 8D**). During the first image the tip appears to have been broken, resulting in the large morphological change seen in **Figure 8B**. In each subsequent image, the tip becomes progressively more rounded, an excellent example of the more common phenomenon of gradual wear (see discussion). The estimated tip radii from the BTR models are included in **Figure 8**.

In contrast, **Figure 8E,F** presents BTR models of a diamond tip probe (see **Table of Materials**) acquired 6 months apart, with thousands of nanoindentations and hundreds of millions of force curve imaging based tip-sample interactions occurring in between. As can be seen from the estimated tip radii of 29 nm (**Figure 8E**) and 28 nm (**Figure 8F**), the probe tip radius did not change within the limits of the BTR method, highlighting the extreme wear resistance of diamond. It should be noted, however, that diamond tip probes (like all AFM probes) are susceptible to contamination from loosely adhered debris that can impact the tip area function and effective hardness. Accordingly, sample cleanliness remains vital for tip preservation and accurate nanomechanical measurements.

### Application examples

Through the judicious choice of probe material composition, cantilever spring constant, and tip geometry and radius, cantilever-based nanoindentation can be used to quantify the nanoscale mechanical properties of materials with elastic moduli ranging from kPa to GPa, both in fluid and under ambient conditions. Selected application examples follow to highlight a few of the wide range of use cases possible for cantilever-based nanoindentation.

### Investigation of loblolly pine mechanical properties for biofuel applications

Loblolly pine trees (*Pinus taeda*) are a fast-growing softwood species that are highly abundant in the southern United States, occupying over 13 million hectares<sup>31</sup>. Because of their abundance, loblolly pine trees are a critical commercial crop in the southern US, commonly used for both timber and pulp wood. Additionally, they are an important resource for second-generation cellulosic biofuels production<sup>32</sup>. Importantly, demand has been growing for

cellulosic biofuel feedstock due to the Energy Independence and Security Act (EISA) of 2007, which mandates that by 2022, total renewable fuel usage in the US transportation industry should be 36 billion gallons, with 16 billion gallons being derived from cellulosic biomass. Accordingly, due to loblolly pine's fast growth rate and amenability to agroforestry projects, it has become a biofuel feedstock of great interest in recent years<sup>33</sup>. Knowledge of the mechanical properties of loblolly pine, including variability across individual trees, anatomical fractions (e.g., whitewood, bark, needles), and cell areas (e.g., cell wall versus interior), may allow for the targeted separation of biomass streams to optimize mechanical processing and thermochemical conversion<sup>34</sup>.

**Figure 9** presents a representative AFM topography (height sensor) image (**Figure 9A**) and corresponding elastic modulus map (**Figure 9B**) of a cross-section sample of whitewood obtained from a branch on a 23-year-old loblolly pine with a ~30 nm radius of curvature diamond tip probe mounted on a stainless steel cantilever ( $k = 256$  N/m). The topography and modulus maps were generated simultaneously using rapid kHz rate force curve-based AFM imaging, with the modulus map presenting semi-quantitative results based on nominal values for the probe calibration constants (i.e., spring constant, deflection sensitivity, and tip radius) and fitting the force curves in real time to the DMT (Derjaguin, Muller, and Toporov) contact mechanics model<sup>35</sup>. Cross-sectioned samples trimmed to be <3 mm in all three dimensions (length x width x height) were prepared for imaging by serial dehydration using increasing concentrations of ethanol (33%, 55%, 70%, 90%, and 100%)<sup>36</sup>, before infiltrating with resin (see **Table of Materials**) and polymerizing at 60 °C overnight. Fully cured resin-embedded samples were first ground, then ultramicrotomed with a diamond blade operating at a cutting

speed of ~1 mm/s with a feed thickness decreasing from 1  $\mu\text{m}$  down to 50-70 nm per slice to produce a flat surface amenable to AFM imaging. However, as can be seen by the color scale bar in **Figure 9A**, the resultant surface in this case is still relatively rough, perhaps due to the presence of residual debris on the sample surface and/or ultramicrotome blade, leading to blade "chatter" during sectioning, whereas other samples exhibited much smoother surface topography.

**Figure 9C** reproduces the AFM topography image from **Figure 9A**, but with white crosshairs indicating the locations for eight arrays of 50 nanoindents apiece to be performed along selected cell walls within the ROI, as the goal of the project in question was to understand how the nanomechanical properties of loblolly pine differ across various tissue types and tree age. A trigger threshold of 1  $\mu\text{N}$  was typically employed for the ramps (60 nm nominal ramp size conducted at a 1 Hz ramp rate), leading to an indentation depth of ~10 nm along the cell walls ( $8 \pm 2$  nm across all samples studied) or slightly deeper ( $14 \pm 4$  nm) in the cell interiors, which are somewhat softer than the cell walls. Indents within each line were spaced  $\geq 100$  nm apart to ensure they were well separated, and 1,024 data points were collected per ramp to produce well characterized approach and retract curves. By combining rapid force curve-based imaging with point-and-shoot cantilever-based nanoindentation, it was possible to generate statistics and determine differences in moduli across cell structures. For example, as shown in **Table 1**, it was found that the average elastic modulus of the cell interior was about half that of the cell wall across whitewood samples derived from multiple branches of trees of varying ages.

Sample	Location	$E^*$ (GPa)	$E$ (GPa)	Deformation (nm)	Count ( $n$ )
1	Interior	$1.5 \pm 0.4$	$1.4 \pm 0.4$	$14 \pm 2$	199
	Wall	$4.7 \pm 1.3$	$4.3 \pm 1.3$	$7 \pm 2$	202
2	Interior	$1.3 \pm 0.3$	$1.2 \pm 0.3$	$16 \pm 3$	198
	Wall	$3.2 \pm 0.9$	$2.9 \pm 0.9$	$9 \pm 2$	199
3	Interior	$1.9 \pm 0.6$	$1.7 \pm 0.6$	$12 \pm 3$	198
	Wall	$5.7 \pm 1.2$	$5.2 \pm 1.2$	$6 \pm 1$	199
4	Interior	$2.4 \pm 0.8$	$2.2 \pm 0.8$	$11 \pm 3$	202
	Wall	$4.2 \pm 2.1$	$3.8 \pm 2.1$	$9 \pm 4$	193
5	Interior	$2.6 \pm 0.8$	$2.3 \pm 0.8$	$10 \pm 2$	198
	Wall	$4.3 \pm 1.6$	$3.9 \pm 1.6$	$7 \pm 2$	199
Average	Interior	<b><math>1.9 \pm 0.6</math></b>	<b><math>1.8 \pm 0.6</math></b>	<b><math>13 \pm 3</math></b>	
	Wall	<b><math>4.4 \pm 1.4</math></b>	<b><math>4.0 \pm 1.4</math></b>	<b><math>8 \pm 2</math></b>	

**Table 1: Loblolly pine elastic modulus statistics: cell walls versus cell interior.** Measured elastic moduli of the cell walls versus cell interiors for five loblolly pine whitewood branch samples collected from two trees of differing ages. All modulus values were calculated by fitting the approach portion of the force displacement curve to the DMT model and assuming a Poisson's ratio of 0.3 for the sample. Moduli are reported as average  $\pm$  standard deviation for each sample location, with the number of force curves (count,  $n$ ) analyzed to produce the reported result indicated. Measured reduced moduli ( $E^*$ ) were converted to actual sample moduli ( $E$ ), assuming a Young's modulus of 1,140 GPa and Poisson's ratio of 0.07 for the diamond tip indenter employed. Also shown is the average sample deformation for the applied load of 1  $\mu$ N.

### Correlated nanomechanics and electron microspectroscopy on Bakken shales

Bakken shale deposits are found within the Williston Basin in Montana and North Dakota in the United States and parts of Saskatchewan in Canada. They are the second largest hydrocarbon reservoir in the United States, but study of the deposits is still in its infancy<sup>37</sup>. An investigation of the nanomechanical properties of Bakken shale as a function of composition and thermal

maturity was conducted by co-localizing AFM cantilever-based nanoindentation with scanning electron microscope (SEM) imaging and energy dispersive spectroscopy (EDS) elemental composition characterization, as shown in **Figure 10**. Specifically, SEM-EDS mapping was used to characterize the elemental distribution (**Figure 10C**), thereby determining the presence and location of various mineral inclusions within the shale matrix. Rapid (kHz rate) force curve-based AFM imaging (**Figure 10B**) was co-localized with the SEM-

EDS maps by defining an optically identifiable origin in the secondary electron (SE) SEM image (**Figure 10A**) and tracking the stage movement of both the AFM and SEM<sup>38</sup>. By again utilizing a diamond tip probe mounted on a stiff stainless steel cantilever, mapping of variations in the elastic modulus was possible for large regions (85  $\mu\text{m}$  x 85  $\mu\text{m}$ ) containing inclusions of interest (**Figure 10D**). Note that the modulus map presented in **Figure 10D** is qualitative rather than quantitative in nature, as the proper probe calibration constants were not entered into the software prior to imaging and data acquisition.

The AFM images in **Figure 10B** and **Figure 10D** also highlight one of the drawbacks of the diamond tip probe employed, namely its inability to accurately track high aspect ratio features (see the black oval region in **Figure 10B**) due to its cube corner tip geometry. The reduced resolution and inability to accurately track steep features can be more clearly seen in **Figure 11**, where the same general area of a Bakken shale sample has been imaged by the cube corner diamond tip (**Figure 11A**) and a significantly sharper, higher aspect ratio stiff tapping mode silicon AFM probe (**Figure 11B**). More specifically, the image shown in **Figure 11B** was acquired with the probe characterized in **Figure 8A-D**, between the BTR models in **Figure 8A** ( $R = 11$  nm) and **Figure 8B** ( $R = 43$  nm). For direct comparison, image pairs **Figure 11C,D**, along with **Figure 11E,F**, present zoomed-in images of the same sample surface features obtained with the diamond tip and silicon probe, respectively, showing the effect of tip geometry and radius on image resolution and fidelity. **Figure 11G** presents a composite 3D image combining the surface topography acquired with the sharp, high aspect silicon probe (**Figure 8A,B**) and the modulus values acquired with the

diamond tip probe (**Figure 8E,F**) encoded as the overlaid colored skin.

In addition to the large images shown in **Figure 10** and **Figure 11**, smaller (10  $\mu\text{m}$  x 10  $\mu\text{m}$ ) rapid force curve-based images were acquired using the fully calibrated diamond tip probe. These images focused on areas with no optically visible inorganic mineral inclusions to investigate the properties of the surrounding organic matrix in more detail. By employing a pixel resolution of 512 x 512 (i.e., ~20 nm x 20 nm sampling pixels), >262,000 individual F-D curves were captured and saved with each 10  $\mu\text{m}$  x 10  $\mu\text{m}$  image, enabling excellent statistics. The F-D data was batch processed and analyzed using the AtomicJ software package<sup>23</sup> to implement the Derjaguin-Muller-Toporov (DMT)<sup>35</sup> contact mechanics model. Following fitting, the data were cleaned to remove curves that resulted in a calculated elastic modulus <0 (non-physical) or >30 GPa (since the study was focused on the non-mineral portion of the shale,  $E \ll 30$  GPa) similar to other studies<sup>39,40</sup>, as well as data with a model fit  $R^2 < 0.7$ . While the  $R^2$  cutoff is somewhat arbitrary, it was chosen to only remove data the model obviously could not accurately fit. With the exception of one outlier that included a large mineral inclusion in the imaging area, the curves removed accounted for less than 0.5% of the total data for each image. A summary of the statistical results can be found in **Table 2**. The calculated elastic moduli vary from 3.5 to 6.1 GPa, within the range of what similar studies have also found<sup>39,40</sup>.

Sample	$E$ (GPa)	Yield After Data Cleaning	Count ( $n$ )
1	$6.1 \pm 3.8$	93.70%	7,36,874
2	$5.1 \pm 2.6$	99.70%	7,84,267
3	$3.5 \pm 1.9$	99.60%	7,83,427

**Table 2: Bakken shales' elastic modulus statistics.** Measured elastic moduli of the organic matrices in three Bakken shale samples of different composition and thermal maturity. Sample 1 is a control, while samples 2 and 3 were annealed for 12 h and 48 h, respectively, to artificially simulate thermal maturation. Elastic moduli are reported as average  $\pm$  standard deviation for each sample location, with the number of force curves (count,  $n$ ) included in the analysis after employing the data cleaning procedure described in the text indicated. The calculated average moduli (3.5-6.1 GPa) fall within the range reported in other similar studies such as that of Li et al.<sup>40</sup>, which found a modulus range of 2.9-11.8 GPa.

### Mesenchymal stem cell nuclear stiffness changes due to external stimuli

Mesenchymal stem cells (MSCs) are progenitor cells that can become chondrocytes, adipocytes, osteoblasts, and myocytes<sup>41</sup>. MSC differentiation into these various tissue types is affected by external mechanical stimuli on the cell via the Linker of the Cytoskeleton and Nucleoskeleton (LINC) complex, which physically links the outer cell membrane to the nuclear membrane<sup>41</sup>. The LINC complex is composed of SUN and Nesprin proteins that interact with the cell cytoskeleton to detect physical forces on the cell and facilitate nuclear import of the mechanosensitive factors  $\beta$ -catenin and YAP to initiate the differentiation process<sup>42,43,44</sup>. Along with the nuclear import of  $\beta$ -catenin and YAP after the mechanostimulation of cells, the cytoskeleton also undergoes rearrangement, including the formation of F-actin filaments around the nucleus as well as the nuclear translocation of actin<sup>44,45,46</sup>. Because mechanostimulation initiates changes to the cell cytoskeleton and nuclear entry of actin, the overall stiffness (modulus) of cells and nuclei is affected and can be measured by AFM cantilever-based nanoindentation. Previous studies have confirmed this by

detecting a decrease in cell and nuclear modulus after disruption of the LINC complex, and inversely an increase in cell and nuclear modulus after the mechanostimulation of MSCs<sup>47</sup>. Current research is still investigating the mechanisms for actin import to the nucleus and how actin polymerization affects cell and nuclear modulus after mechanostimulation.

To investigate the mechanical properties of live cells, the experiments must be conducted in a buffer solution, typically PBS. Conducting cantilever-based nanoindentation in fluid poses unique problems, specifically for the measurement of very soft samples such as MSCs ( $E \approx 2$  kPa). In particular, the low elastic moduli of living cells necessitates the use of a large probe radius to reduce the stress imparted on the cell structure and avoid puncture of the membrane. Additionally, very low spring constant cantilevers ( $k = 0.04$  N/m) are necessary to measure such low elastic moduli, but this increases the probability of false engaging due to the viscous drag of the fluid, leading to deflection of the soft cantilever during the initial fast lowering step of the AFM engage process. To counteract the higher propensity

for false engages, it may be necessary to utilize a larger engage setpoint (i.e., deflection voltage trigger threshold to end the engage process). Since softer cantilevers can generally be elastically deformed to a greater extent than stiff cantilevers, the greater bending experienced with a higher engage setpoint in fluid is generally not detrimental to such soft probes. In addition, it is imperative that the solutions used in a fluid environment are free of debris and bubbles, as floating debris or bubbles can transiently interfere with transmission of the laser through the fluid to the PSD or adhere to the cantilever and block the laser. Interference with the laser beam will negatively impact the resultant F-D curves and often results in false crash detection or false engaging. Finally, nanoindentation on live cells also requires more user input than on harder, inanimate materials. In particular, because the cells and their fluid environment are much more dynamic, it may be necessary to actively adjust the height of the probe for each ramp to ensure a good F-D curve is obtained.

In live cell nanoindentation, much larger sample deformation is often needed to result in the same cantilever deflection relative to stiffer samples. This larger deformation can result in experimental results deviating from the Hertz model's assumption of linear elasticity, and hence a correction factor may need to be applied to account for the hyperelastic behavior for accurate F-D analysis<sup>48</sup>. It has been found that the geometric size ratio  $\beta = \frac{R_2}{R_1}$ , where  $R_2$  is the radius of the indenter and  $R_1$  is the radius of the cell (see **Figure 12A**), can be used to predict the resulting data's adherence to Hertzian mechanics. The ideal geometric size ratio has been found to be  $\beta = 0.3$ , with  $\beta$  values  $<0.3$  leading to underestimating the elastic modulus and  $\beta$  values  $>0.3$  leading to overestimating the elastic modulus when analyzed

with Hertz contact theory<sup>48</sup>. One common way to avoid nonlinear effects is to keep deformations small. In this study, the indentation depth was limited to 500 nm-1  $\mu$ m.

A representative data set showing results of a single set of nanoindentation experiments on MSCs and isolated nuclei is shown in **Figure 12B**. In the data presented in **Figure 12B**, precalibrated (spring constant *via* LDV and tip radius *via* SEM), 5  $\mu$ m radius hemispherical probes with a nominal spring constant of  $k = 0.04$  N/m were used to investigate differences in modulus between intact live MSCs and isolated MSC nuclei, which served as controls to test the effects of static and dynamic strains on cell and nuclear mechanical properties<sup>46</sup>. Due to differences between and challenges in engaging on the cells and nuclei, the extracted modulus data tends to exhibit a large variation (i.e., distribution of values). Accordingly, the dataset in **Figure 12B** presents a 75<sup>th</sup> percentile of the data collected. Due to this innate variability among live cells and resultant measurement spread, it is recommended to conduct replicate nanoindentation experiments on large numbers of samples with at least three biological replicates in order to generate robust statistics for data analysis and interpretation<sup>30</sup>.

### Mechanical properties of cholesterol-containing lipid bilayers

Supported lipid membranes with very high (>50 mol%) cholesterol (Chol) content, typical of the composition found in eye lens membranes, were prepared and incubated on freshly cleaved muscovite mica<sup>49</sup>. A representative AFM topography image of such a supported lipid membrane (SLM) prepared at a Chol/POPC (POPC = 1-palmitoyl-2-oleoyl-glycero-3-phosphocholine) mixing ratio of 1 is shown in **Figure 13A**, with the height profile along the purple line in the image

shown below the figure. The SLM in **Figure 13A** completely covered the exposed mica surface with sufficient incubation time (~25 min) and a sufficient lipid concentration (0.3 mg/mL), as evidenced by the lack of distinguishable features in the topography image. Likewise, the height profile across the image provides structural details regarding the roughness of the membrane surface, with the SLM smooth as expected.

**Figure 13B** presents a collection of approach sections of force curves captured on the SLM shown in **Figure 13A**. To achieve better statistics regarding the mechanical properties of the SLM, force curves were collected at equidistant points spaced at least 100 nm apart, covering almost the entire width of the SLM. The spacing between points ( $\geq 10\times$  the indentation depth) was chosen to prevent indenting from occurring too close together. The force curves show a clear breakthrough event, as evidenced by the discontinuity or sudden jump between the ~0 and ~5 nm separation distances in the approach section of the force curves where the force drops precipitously from ~10 nN to ~5 nN. The average breakthrough force for the membrane shown in **Figure 13A** (Chol/POPC mixing ratio of 1) based on the approach curves in **Figure 13B** is calculated to be  $9.25 \pm 0.27$  nN.

In contrast, **Figure 13C** shows an AFM topography image of the partial membrane or membrane patches formed by again incubating membranes at a Chol/POPC mixing ratio of 1, but at a much lower concentration of lipids (~15  $\mu\text{g/mL}$ ) and with a shorter incubation time (~5-6 min)<sup>49</sup>. The height profile along the red line across the membrane patch in the center of the image is shown below the figure. The measurement across the partial bilayer provides the thickness of the SLM,

shown by the black dashed lines in **Figure 13C** to be ~7 nm. However, this measured thickness also incorporates a 1-2 nm water layer between the membrane and the mica disk<sup>50</sup>. It should be noted that the partial membrane is often only weakly attached to the mica surface, which can cause lipid particles to be removed from the edge of the partial membrane patches during scanning, but a slightly longer incubation time or lowering the imaging force can eliminate this difficulty.

Calibration of the AFM probe is crucial to accurately quantify SLM mechanical properties. In particular, although the tip spring constant remains consistent in air or fluid medium, the deflection sensitivity must be calibrated in the same medium where experiments are performed. It is critical to calibrate the deflection sensitivity immediately before each set of force curve acquisitions to ensure reproducible results, as the laser alignment and/or reflectivity of the backside coating can change over time, particularly in fluid. Very sharp probes are discouraged for capturing membrane force curves, as they easily puncture the SLM and might lead to measuring an erroneously low breakthrough force or no breakthrough at all. However, repeated use of the same tip without proper cleaning increases the chance of debris accumulating on the tip and thereby dulling the tip or affecting the tip-sample adhesive forces. A lack of breakthrough events evident in the approach force curves may also correspond to pushing only on mica rather than the actual membrane; thus, visual confirmation of membrane formation before capturing force curves is necessary.



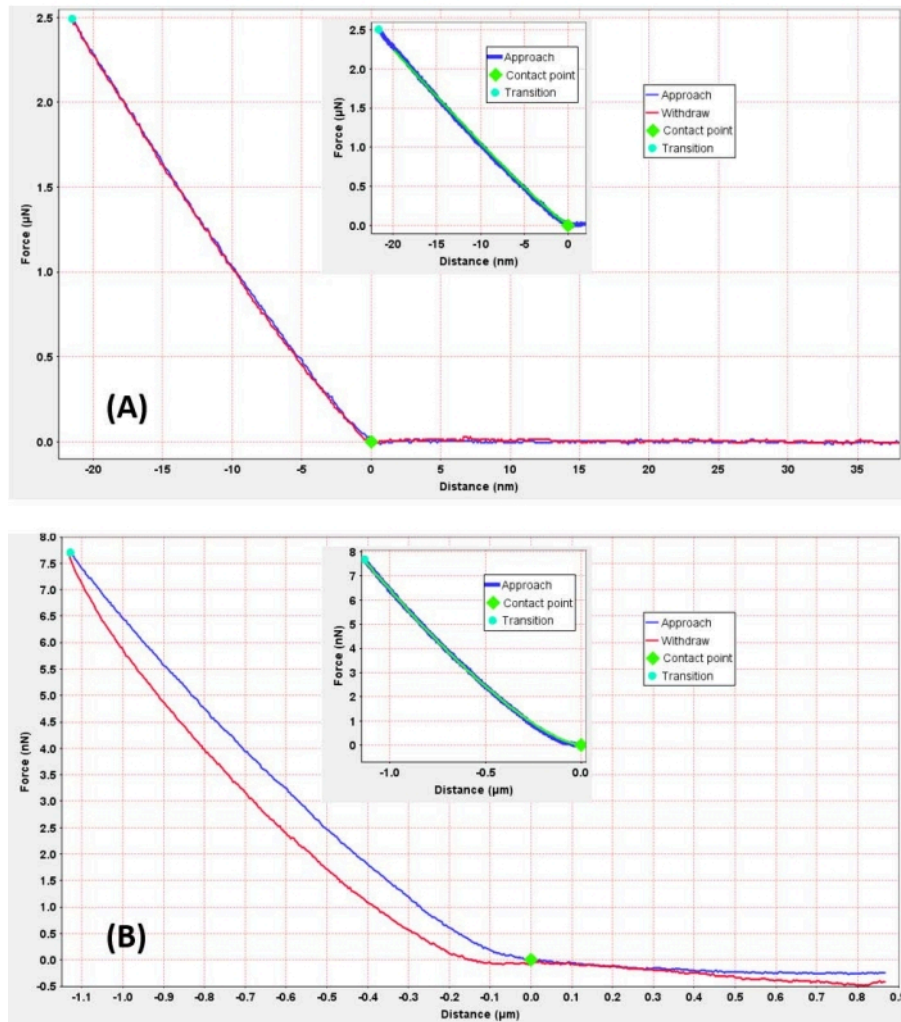


**Figure 7: Representative force-displacement (F-D) curves in air and fluid.** Representative force curves obtained on (A) a loblolly pine in air with accompanying DMT model fit, and (B) a live MSC nucleus in PBS with an accompanying Hertz model fit. Insets in panels A and B show a zoom of the contact region of the corresponding approach curves (blue traces) with accompanying fit (green traces). In each panel, the initial tip-sample contact point (as determined by the fitting algorithm) is indicated by a green diamond, while the turn-around point (i.e., transition from approach to retract or withdraw) is indicated by a cyan circle. [Please click here to view a larger version of this figure.](#)

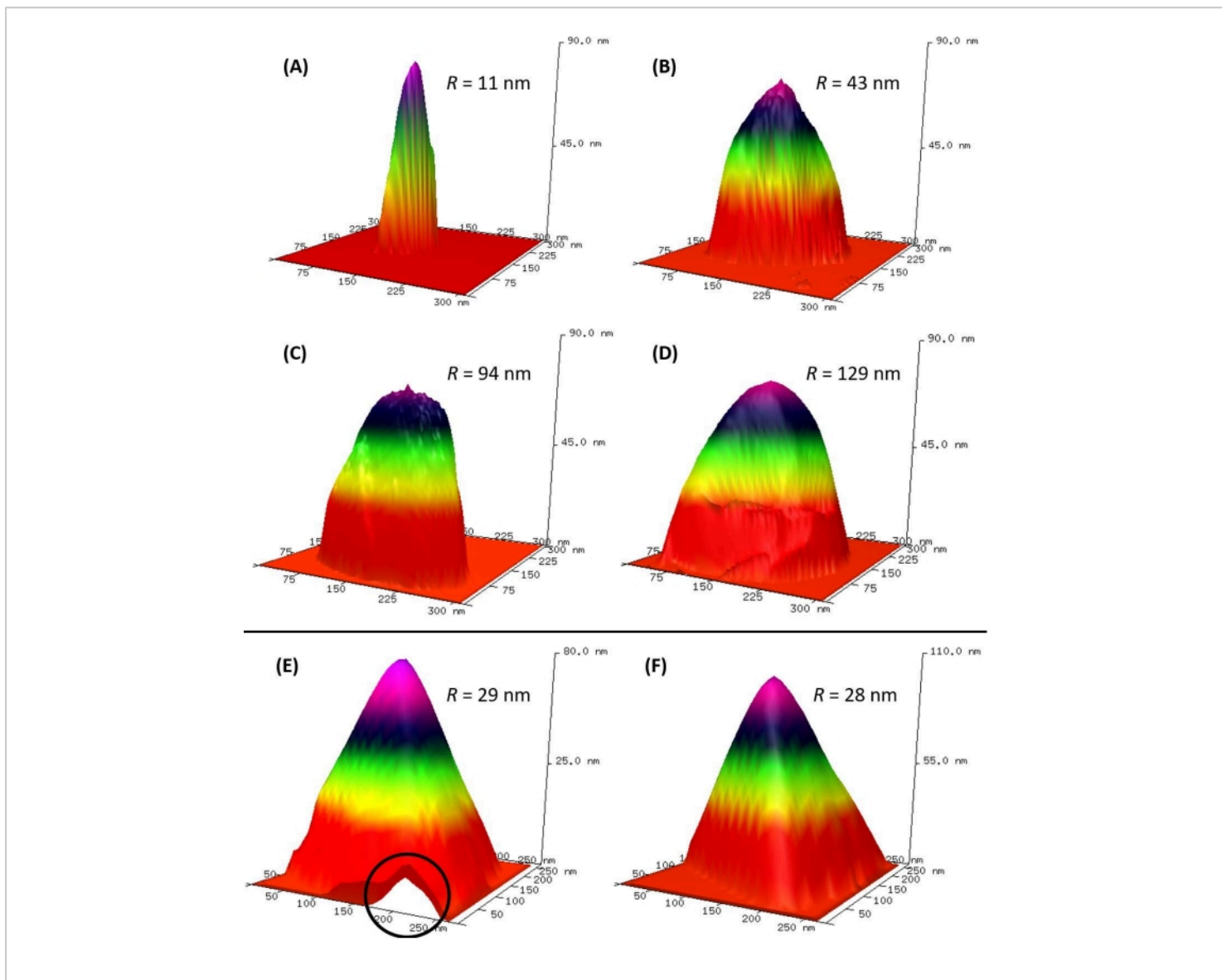


**Figure 8: Comparison of silicon versus diamond probe tip wear. (A-D)** Silicon probe tip. Series of models created by the blind tip reconstruction method following imaging of a tip characterization sample, demonstrating the evolution in radius of a stiff cantilever silicon tip probe (see **Table of Materials**) due to progressive tip wear experienced over the course of three sequential  $85\ \mu\text{m} \times 85\ \mu\text{m}$  ( $1024 \times 1024$  pixels) force curve-based images of a Bakken shale sample, conducted at a line scan rate of 0.1 Hz and force curve sampling rate of 2 kHz (i.e.,  $\sim 20$  million tip-sample interactions/image). **(A)** Tip as received (out of the box), prior to use.  $R = 11\ \text{nm}$ . **(B)** Tip after one image ( $R = 43\ \text{nm}$ ). **(C)** Tip after two images ( $R = 94\ \text{nm}$ ). **(D)** Tip after three images ( $R = 129\ \text{nm}$ ). **(E,F)** Diamond probe tip. BTR models of the same diamond tip probe (see **Table of Materials**) obtained  $\sim 6$  months apart. Between acquisition of the tip images used to generate the models shown in **E** and **F**, thousands of nanoindents were performed with the probe and hundreds of millions of tip-sample interactions during force curve-based imaging occurred. Nevertheless, due to the hardness of diamond, the estimated tip end radius of  $\sim 30\ \text{nm}$  did

not change within the uncertainty limits of the BTR technique between acquisition of the initial (**E**) and follow-up (**F**) images of the tip. The asperity observed in the earlier model (indicated by the black circle in panel **E** is most likely either an artifact of the BTR method or due to the presence of a nanoscale contaminant (e.g., dust particle) on the side of the tip. [Please click here to view a larger version of this figure.](#)

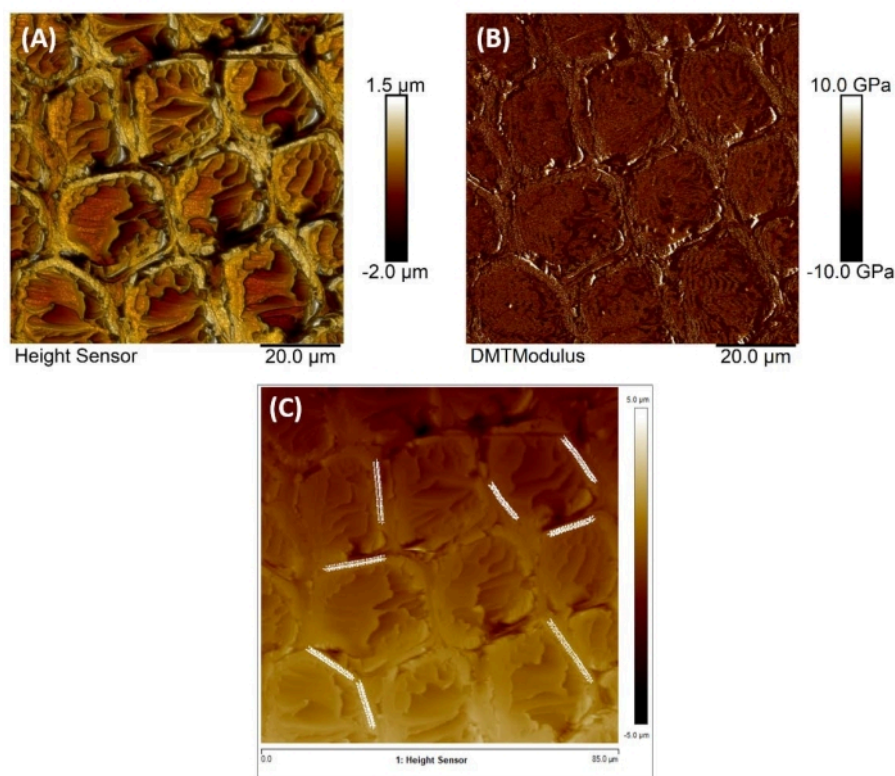


**Figure 9: AFM topography and modulus maps of a loblolly pine sample.** Representative AFM data acquired in air on a cross-sectioned loblolly pine sample embedded in resin to enable cantilever-based nanoindentation measurements on cell walls. **(A)** AFM topography image covering multiple cells acquired *via* a rapid force curve-based imaging mode, presented as a pseudo-3D depiction. **(B)** Elastic or Young's modulus map generated in real time by the AFM software by analyzing the force curve acquired at each pixel and fitting the data to the DMT model, showing that the cell walls are stiffer than the cell interiors. Note that the nominal, rather than measured, probe calibration parameters were used, so the modulus values should be treated as qualitative or only semiquantitative. **(C)** Overview of the ROI indicating the locations (eight lines consisting of 50 white crosshairs apiece spaced  $\geq 100$  nm apart) where 400 nanoindents (60 nm nominal ramp size, with a 1  $\mu\text{N}$  trigger threshold corresponding to an average indentation depth of  $\sim 10$  nm) were performed along selected cell walls following acquisition of the AFM image to enable the locating of indents with nanoscale precision. Scale bars = 20  $\mu\text{m}$  **(A,B)**. Abbreviations: AFM = atomic force microscopy; DMT = Derjaguin-Muller-Toporov. [Please click here to view a larger version of this figure.](#)

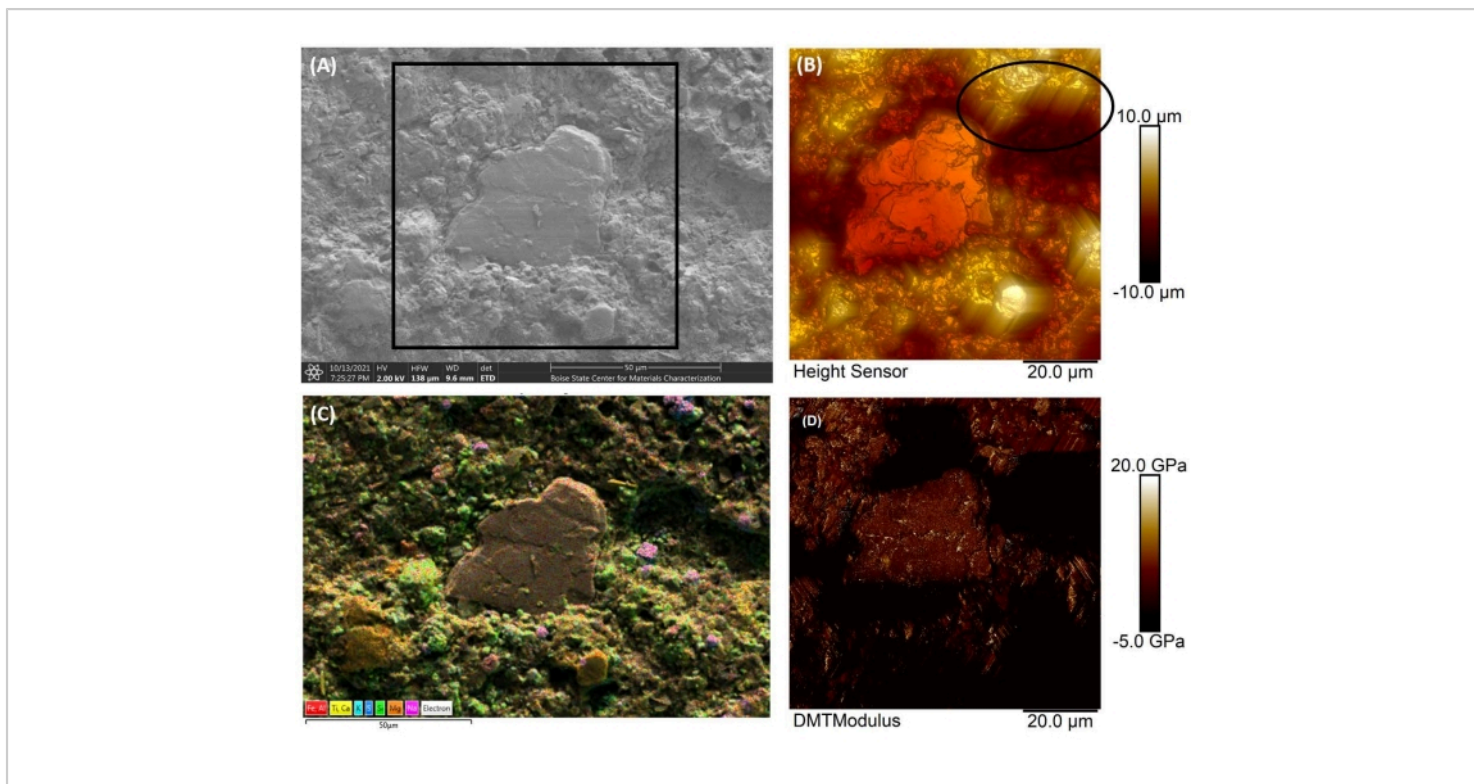


**Figure 10: Co-localized AFM and SEM/EDS of a Bakken shale sample.** (A) Secondary electron SEM image of a portion of a Bakken shale sample. (B) AFM topography image of the region indicated by the black box in A. Black oval indicates a region where the low aspect ratio of the probe leads to imaging of the probe sidewall rather than the steep, high aspect ratio surface topography feature. (C) EDS elemental composition map obtained for the SEM image shown in A. (D) AFM-derived elastic or Young's modulus map generated in the course of obtaining the AFM topography image in B, showing the mineral inclusion in the center of images A-D is significantly harder than the surrounding organic matrix. Scale bars = 50 μm. Abbreviations: AFM = atomic force microscopy; SEM = scanning electron microscopy; EDS = energy dispersive spectroscopy. [Please click here to view a larger version of this figure.](#)

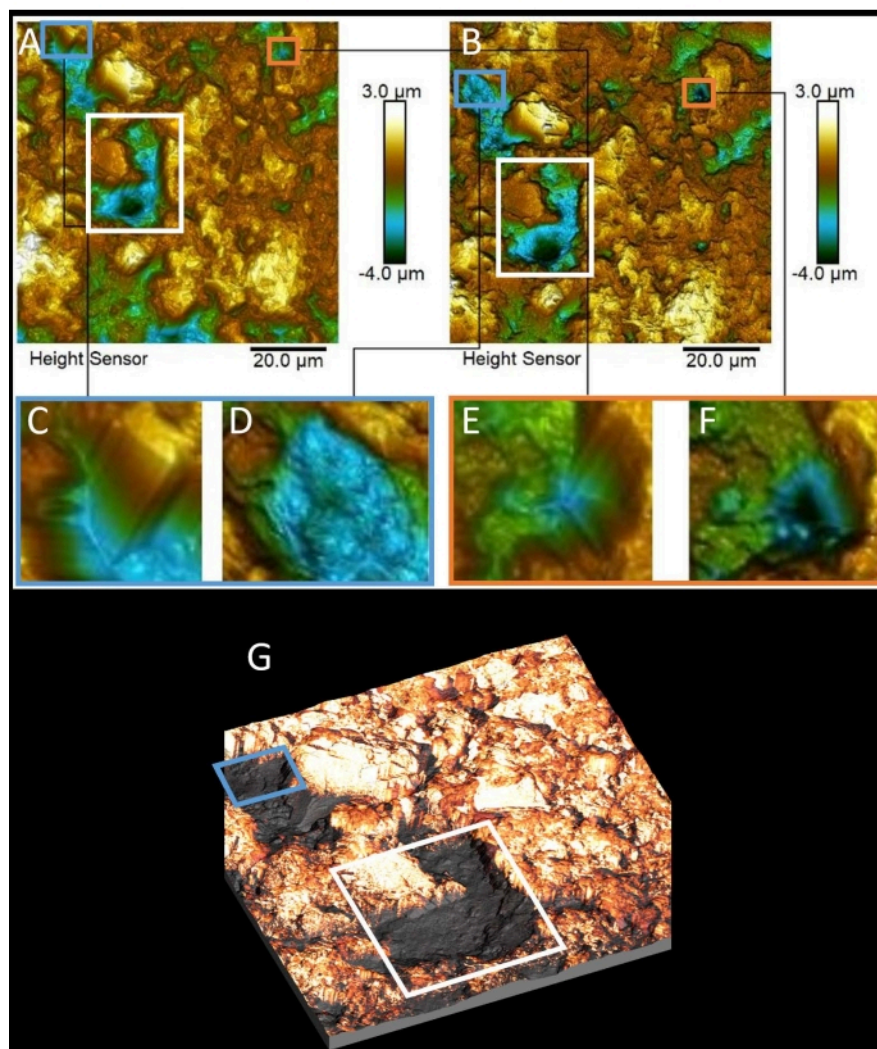


**Figure 11: Effect of probe tip radius and shape on the appearance of high aspect ratio features.** Comparison of feature resolution obtained using either (A) an  $R \approx 30$  nm low aspect ratio (tip half angle =  $47^\circ$ ) diamond tip probe (see **Table of Materials**) or (B) an  $R \approx 10$  nm high aspect ratio (tip half angle  $\approx 19^\circ$ ) stiff silicon probe (nominal  $k = 200$  N/m; see **Table of Materials**) to image the same location on a Bakken shale sample. (C-F) Zoomed-in images of the blue (C,D) and orange (E,F) boxed regions in A and B obtained with either the larger radius of curvature low aspect ratio diamond tip probe (C,E) or the sharper, higher aspect ratio stiff silicon tapping mode probe (D,F), highlighting the decreased feature resolution and introduction of tip sidewall artifacts in the AFM topography image obtained with the diamond tip probe due to its larger tip radius and half angle. The areas highlighted in C-F contain steep, deep well-like features that demonstrate the trade-offs in terms of lateral resolution, accurate tracking, and image fidelity between a more easily dulled, initially sharp silicon probe or a blunter, wear-resistant diamond tip probe. (G) Composite 3D image generated by combining AFM topography acquired with the sharp, higher aspect ratio stiff silicon probe with modulus data (overlaid colored skin) derived from rapid force curve

imaging of the same area of the sample with the diamond tip probe. The features highlighted by the blue and white boxes in **A** and **B** are indicated in **G** as well. [Please click here to view a larger version of this figure.](#)

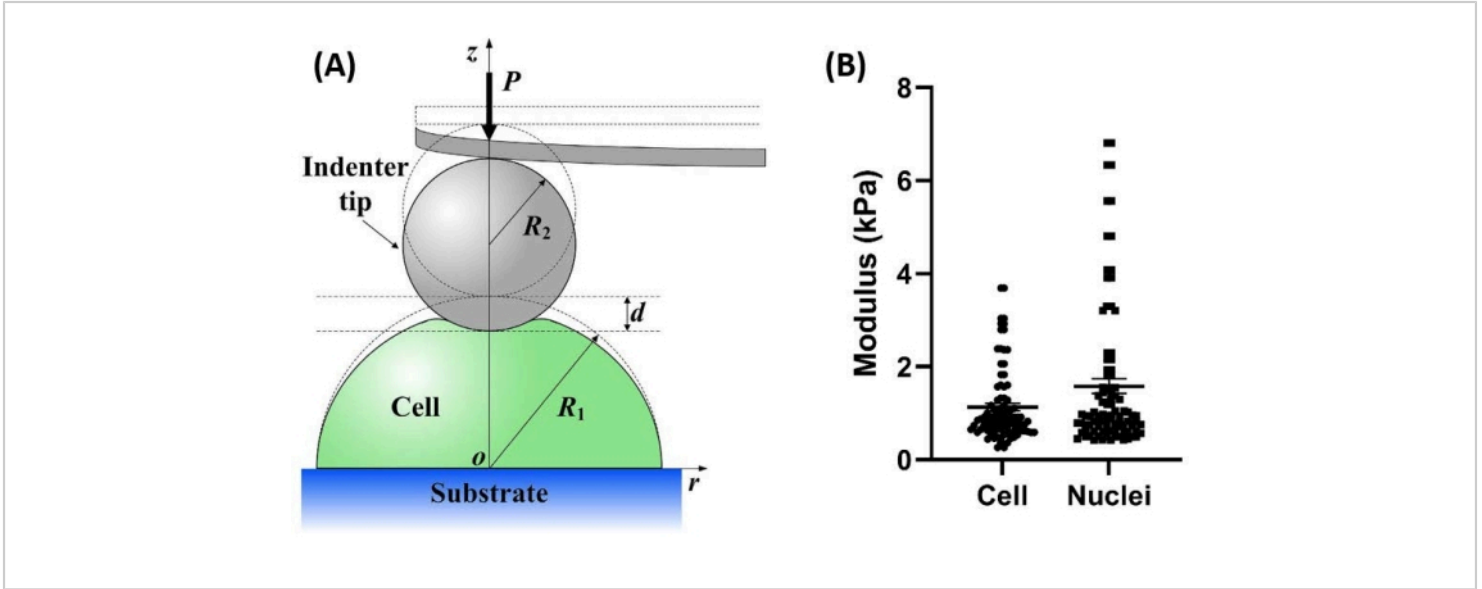


**Figure 12: Cantilever-based nanoindentation on cells or nuclei.** (A) A cell with radius  $R_1$  located on a flat, rigid substrate is indented to a depth  $d$  by a spherical indenter with radius  $R_2$ . This figure was reproduced from Ding et al.<sup>48</sup>. (B) Individual value plots of representative modulus measurements obtained from AFM cantilever-based nanoindentation experiments on mouse MSCs and isolated nuclei extracted from mouse MSCs. A total of 10 cells and 10 nuclei were measured five times each at an indentation depth of 500-600 nm (chosen to permit usage of the Hertz contact mechanics model). The resultant raw F-D curve data was processed using Atomic J<sup>23</sup> to calculate the elastic moduli. Due to the large innate variability of the cells, a 75<sup>th</sup> percentile of the data is plotted. Cell and isolated nuclei exhibited no statistical difference in elastic modulus, with a measured average moduli of  $0.75 \pm 0.22$  kPa and  $0.73 \pm 0.22$  kPa, respectively. Similar data have been collected and analyzed to determine differences in nuclear stiffness due to mechanical stimulation, protein knockouts, and chemical treatments. Abbreviations: MSC = mesenchymal stem cell; AFM = atomic force microscopy; F-D = force-displacement.

[Please click here to view a larger version of this figure.](#)

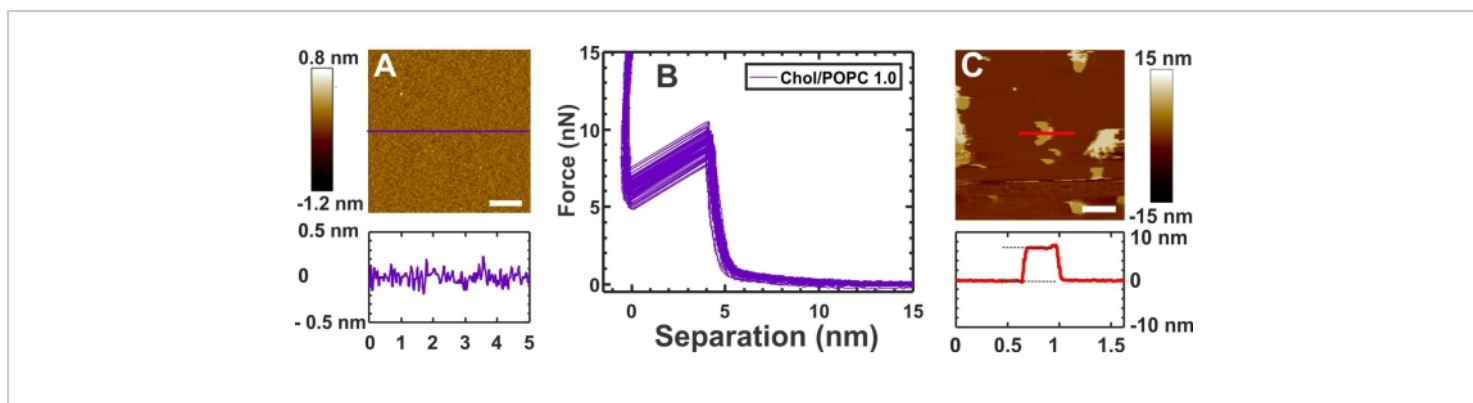


**Figure 13: Morphology and nanomechanical properties of lipid bilayers.** (A) AFM topography image showing the minimal height variation of a complete supported lipid membrane (SLM) composed of Chol/POPC at a mixing ratio of 1 that formed across the entire exposed mica surface with a long incubation time (~25 min) and high lipid concentration (0.3 mg/mL). The height profile along the purple line across the middle of the image is shown below the figure, providing structural details of the membrane surface. As expected, the SLM is extremely smooth. (B) Collection of approach sections of force curves captured on the SLM shown in A. Force curves were collected at equidistant points  $\geq 100$  nm apart covering almost the entire SLM. The force curves show a clear breakthrough event, as evidenced by the discontinuity or sudden jump in the approach section of the force curves. The average breakthrough force is  $9.25 \pm 0.27$  nN. (C) Partial membrane or membrane patches formed by incubating membranes at a Chol/POPC mixing ratio of 1 with a shorter incubation time (~5-6 min) and lower lipid concentration (~15  $\mu\text{g/mL}$ ) relative to A<sup>49</sup>. The height profile along the red line on the patch is shown below the image. The partial bilayer enables measurement of the thickness of the SLM, shown by the black dashed lines in the height profile. Note that the measured thickness also incorporates a 1-2 nm water layer between the membrane and the mica disk<sup>50</sup>. This figure was adapted from Khadka et al.<sup>49</sup> with permission from Elsevier. [Please click here to view a larger version of this figure.](#)

## Discussion

### Sample preparation

For nanoindentation in air, common preparation methods include cryosectioning (e.g., tissue samples), grinding and/or polishing followed by ultramicrotoming (e.g., resin-embedded biological samples), ion milling or focused ion beam preparation (e.g., semiconductor, porous, or mixed hardness samples not amenable to polishing), mechanical or electrochemical polishing (e.g., metal alloys), or thin

film deposition (e.g., atomic layer or chemical vapor deposition, molecular beam epitaxy). The goal is to create a sample with minimal surface roughness (ideally nm-scale,  $\leq 0.1 \times$  the intended indentation depth). With many of the preceding methods, the sample may need to subsequently be rinsed with and/or sonicated in high purity filtered (e.g., HPLC grade) solvent and dried with ultrahigh purity (99.999%) nitrogen ( $\text{N}_2$ ) gas to remove particulate debris. Alternatively, flakes (e.g., 2D materials) or particles (e.g., nanoparticles or microcapsules) can be spin coated or



drop cast out of solutions prepared using high purity filtered solvents. In this case, the goal is to achieve a surface density that yields multiple non-overlapping flakes or particles within the field of view in any randomly chosen area on the sample. For nanoindentation in fluid (often employed for biological samples requiring buffer solution to remain viable), deposition or preparation of samples on a smooth (nanometer-scale surface roughness) substrate (e.g., microscope slide, Petri dish, or freshly cleaved muscovite mica) is necessary<sup>46,47,49</sup>.

### Probe selection considerations

The selection of an appropriate probe is of the utmost importance for quantitative analysis of F-D curves, as the tip-sample interaction is the fundamental property being measured in cantilever-based nanoindentation. The following questions are of particular importance when choosing a probe for a given experiment. What is the sample's expected (or measured) surface roughness and elastic modulus range? High roughness samples can cause accelerated wear compared to smoother samples due to the increased lateral forces present on the tip when tracking steep features, as well as increase the likelihood of tip break events<sup>53</sup>. Likewise, the harder the sample is, the faster it will wear the probe tip. In addition, how many images and/or nanoindents are necessary? With less imaging and indenting, less tip wear can be expected. As described in greater detail below, tip wear can be decreased by utilizing diamond-like carbon (DLC) coatings or virtually eliminated by using diamond tip probes (with the high cost of acquisition offset over time by the nearly infinite probe lifetime).

Another consideration in choosing an appropriate probe is the size of the features of interest. For nanoindentation, it is often best to use the largest tip size possible while maintaining the

spatial resolution needed for the sample(s) in question and desired information content, because larger tips are less likely to experience sudden tip geometry changes due to fracture and will also exhibit lower wear rates<sup>54</sup>. It is also important to consider whether there are other AFM methods to be co-localized with nanoindentation, such as conductive AFM<sup>55</sup>, Kelvin probe force microscopy (KPFM)<sup>56</sup>, or magnetic force microscopy (MFM)<sup>57</sup>. If additional metrologies such as these are to be utilized, the probe tip may need to be electrically conductive or magnetic, which will impact material composition and hence a host of properties, including hardness, wear resistance, and tip radius. Likewise, if indentation will be performed in fluid, the composition of the probe's reflective backside coating (if present) is another important consideration, as it must be corrosion-resistant (e.g., an Au backside coating is common for fluid probes). Finally, and perhaps most importantly, the probe cantilever's spring constant must be matched to the expected range of elastic moduli to be measured. If the spring constant does not match well with the sample modulus, one of two cases may occur. If the cantilever is too stiff, little or no deflection will be measured and characterization becomes impossible; conversely, if the cantilever is too soft, it will not be able to deform the sample enough to measure its mechanical properties.

### Tip wear

Wear can be defined in numerous ways; for the discussion of AFM probe tip wear here, it will be defined as any change in surface topography of the probe tip due to plastic deformation without any loss of material, as well as any removal of material from the surface due to physical interactions<sup>58</sup>. In a broader sense, wear may also involve chemical reactions such as oxidation and hydration. In normal AFM applications, the lateral spatial resolution is usually

limited by the tip radius<sup>59</sup>, and the tip-sample interaction is the primary measured property. Since the tip radius is a key parameter in modeling the contact mechanics of the tip-sample system and subsequently determining the mechanical properties, tip wear is of particular concern when performing nanoindentation experiments and is a key limitation for the accurate interpretation of nanoindentation results<sup>53</sup>. Due to the normally gradual nature of tip wear (aside from tip breakage events), it is not possible to quantify tip wear due to a single nanoindentation cycle (i.e., ramp). In addition, the perpendicular movement of the probe tip relative to the sample in nanoindentation (discounting rapid force curve-based imaging) lends itself to reducing the rate of wear, as the primary mode of tip wear is typically shear forces developing during scanning modes<sup>60</sup>. As such, the primary source of tip wear in nanoindentation experiments is any imaging performed after the initial probe calibration (in particular, deflection sensitivity and tip radius measurements) but before nanoindentation. It is therefore recommended that if silicon or silicon nitride probes are used, the tip radius should be checked both before and after each experiment to monitor and account for any tip wear using one of the methods described above (e.g., SEM analysis or BTR).

## Probe materials

### Diamond-like carbon (DLC)

Through the use of DLC-coated probe tips or diamond tips, tip wear can be vastly reduced or negated altogether<sup>53</sup>. The enhanced wear resistance of these alternative tip materials is very enticing for the measurement of mechanical properties, particularly of very stiff materials. It has been shown that DLC probe tips can show a 1,600-fold increase in wear resistance compared to normal silicon probe tips<sup>54</sup>. This dramatic increase in wear resistance can be attributed to several factors. First, the bonds present in DLC (C-C and

C=C) and its interface with silicon (Si-O, Si-C) are some of the strongest bonds of any elemental pairs, and much stronger than the Si-Si bonds present in silicon tips. DLC also has the effect of decreasing friction, which in turn lowers the shear stresses within the tip, thereby reducing wear. Additionally, the DLC surface chemistry is different from that of a silicon tip, as silicon tips can experience tribochemical etching in ambient humidity conditions, while DLC tips do not (or at least not in any meaningful way compared to the primary wear mode)<sup>54</sup>. The primary downside of DLC-coated tips (beyond increased price relative to standard uncoated silicon tips) is the increased tip radius due to the coating itself. Most DLC probe tip radii are  $\geq 30$  nm, whereas non DLC-coated tips can reliably reach 1-2 nm in radius<sup>61</sup>. However, a larger tip radius can often be desirable for nanoindentation experiments to reduce error in property measurements, as nanoscale discrepancies between the ideal area-depth function and the actual area-depth function, due to probe defects or asperities, will disproportionately affect measurements made with smaller radius probes due to the larger relative error. In addition, despite its superior wear resistance, the DLC coating may eventually wear through in spots, leading to differential wear between the exposed silicon core and the remaining DLC coating. Unfortunately, the wear resistance of the DLC coating may also be limited by the adhesion of the coating to the silicon tip rather than the actual hardness of the coating alone.

### Diamond

Diamond is well known as one of the hardest and most wear resistant materials on Earth. Nevertheless, it has been demonstrated that significant wear can still occur in diamond tips when using large (60  $\mu$ N) forces in a deliberate attempt to explore tip wear<sup>62</sup>. Conversely, in normal nanoindentation and imaging scenarios where the

forces exerted on the tip are much less, there have been no rigorous studies of diamond tip wear. However, as seen in **Figure 8E,F**, BTR modeling of the same diamond probe tip under identical conditions on the same tip characterization sample 6 months apart generated virtually indistinguishable tip shape models (i.e., no discernible evidence of wear). Between the first and second BTR images, the probe was used to perform thousands of nanoindents and underwent hundreds of millions of tip-sample interactions while imaging a variety of stiff materials ( $E > 15$  GPa), including wood (loblolly pine), shale, highly ordered pyrolytic graphite (HOPG), and various graphene thin films. Significantly, the estimated tip radius changed by  $\sim 1$  nm between the two images in **Figure 8E,F**, which is well within the BTR method's error<sup>63</sup>. While not a full study, this comparison demonstrates the excellent durability of a diamond probe under normal experimental nanoindentation (and even imaging) conditions. The major drawbacks associated with the use of diamond tips (beyond expensive up-front cost) are the increased tip radius and, in some ways of more concern, the low aspect ratio of the cube corner geometry of most commercially available diamond tips. **Figure 11A,B** presents side-by-side, comparative AFM images of the same area of a Bakken shale sample acquired with a sharp silicon probe with a nominal tip radius of 8 nm and average half angle of  $\sim 19^\circ$  versus a diamond tip probe with a nominal tip radius of 40 nm and average side angle of  $47^\circ$ . When the enlarged areas are compared (**Figure 11C,D** and **Figure 11E,F**), it is readily evident that the diamond tip probe is unable to resolve and accurately track the steeper (higher aspect ratio) features within the image. Instead, where steep features are present, the tip sidewall makes contact with the upper edge and the AFM system essentially tracks the sidewall of the probe until the tip end makes contact with the surface again and normal tracking resumes.

### Spring constant/modulus matching

As mentioned above, the probe cantilever's spring constant must be matched to the expected range of elastic moduli to be measured. To aid in choosing an appropriate probe, **Table 3** presents suggested approximate nominal cantilever spring constants suitable for selected wide ranges of expected sample elastic moduli ranging from few MPa to 100 GPa in the case of  $\sim 30$ – $40$  nm radius probe tips often employed for nanoindentation<sup>52</sup>. Lower spring constant probes ( $k < 0.1$  N/m) are available for even softer materials (kPa range) such as cells.

Spring Constant (N/m)	Expected Sample Modulus Range
0.25	≤ 15 MPa
5	5 – 500 MPa
40	200 – 8,000 (0.2 – 8 GPa)
200	1,000 – 50,000 (1 – 50 GPa)
450	10,000 – 100,000 (10 – 100 GPa)

**Table 3: Ideal probe spring constants for measuring various modulus ranges.** Approximate nominal probe spring constants for optimal measurement of elastic moduli across varying ranges from few MPa to 100 GPa, assuming a typical probe radius of ~30-40 nm<sup>52</sup>.

In addition to the spring constant, in the special case of biological materials, the tip radius and forces applied during imaging and nanoindentation must be carefully considered to avoid damage. In the **application example** involving measurement of the mechanical properties of cholesterol-containing lipid bilayers, presented in the representative results section, a relatively sharp (10 nm) tip was specifically used for the analysis of the breakthrough force in lipid bilayers. In contrast, if the material ROI is large enough (e.g., as is the case for cells and cell nuclei) and there is concern regarding the potential for puncture, larger micron-scale hemispherical tips, like those used in the stiffness measurements on MSC nuclei described in one of the **application examples** in the representative results section are ideal and provide excellent results for soft, fragile samples such as live cells and isolated nuclei. Kain et al. present an in-depth discussion of how to choose the optimal combination of probe radius and spring constant to achieve the highest possible measurement sensitivity for such samples<sup>64</sup>.

### Probe calibration

#### Deflection sensitivity

The deflection sensitivity relates movement of the Z-piezo (and thus deflection of the cantilever when indenting on an infinitely stiff substrate, assuming operation in the limit of small deflections) to a measured change in voltage on the PSD<sup>65</sup>. The deflection sensitivity (also sometimes referred to as the inverse optical lever sensitivity [InvOLS]) may be reported in nm/V or V/nm. An overview of the most common deflection sensitivity calibration methods is provided below.

#### Hard surface contact

The easiest and most popular method for determining the deflection sensitivity of the beam bounce laser/AFM probe/PSD system is the aptly named the "hard surface contact" method<sup>65</sup>. Its simplicity, ease of integration into AFM control software workflows, and *in situ* nature all add to the hard surface contact method's appeal and widespread use. To implement this method, the AFM probe tip is ramped against a material much stiffer than the cantilever. The slope of the in-contact portion of the force-displacement curve (displayed as Volts of vertical deflection error signal on the PSD as a function of Z-piezo movement in nm or applied voltage) then gives the deflection sensitivity (**Figure 3A**). The use of

a stiff substrate ensures that all of the measured deflection arises from the cantilever bending rather than a convolution of sample deformation and the cantilever's displacement. In the case of soft cantilevers (e.g.,  $k < 10$  N/m), silicon ( $E \approx 170$  GPa)<sup>27</sup> or mica<sup>17</sup> are easily accessible and readily used materials (or alternatively glass,  $E \approx 70$  GPa, or suitably hard plastic in the case of cells immobilized on a microscope slide or Petri dish), while for stiffer cantilevers, such as those used for some nanoindentation experiments (e.g.,  $k > 200$  N/m; **Table 3**), sapphire ( $E \approx 345$  GPa)<sup>26,66</sup> may need to be used to ensure no sample deformation occurs. Because this method is dependent on the force-displacement measurement, the AFM scanner's Z-piezo must either employ a closed loop height sensor or be well calibrated (if operating in open loop mode) using a variety of height standards. The largest contributor to error in the hard surface contact method is movement of the laser spot on the cantilever due to thermal fluctuations. Changes in the temperature of the cantilever are most commonly caused by the detection laser, although Joule heating in the surrounding electronics may also contribute. Overall temperature differences of 6 °C between the cantilever and ambient air have been reported, which can lead to laser spot shifts of several microns<sup>67</sup>. To account for any heating, it is advisable to wait  $\geq 30$  min after the initial laser spot alignment to allow the cantilever to come into thermal equilibrium with its surroundings for the best and most accurate results. Averaging the slopes of the approach and withdraw curves for each sensitivity measurement will account for any tip friction or sliding effects and should be enacted if possible<sup>68</sup>. Additionally, averaging across multiple sensitivity measurements will help gauge the reliability and reproducibility of the measurement. Good sensitivity measurements should result in deviations of  $\leq 1\%$  and be performed at approximately the same deflection as the expected experimental nanoindents to maximize the

effectiveness of the calibration<sup>69</sup>. The major drawback of the hard surface contact method is that the physical contact necessary for the calibration can potentially cause damage to fragile silicon tips (e.g., dulling or creation of tip artifacts such as a double tip).

### Thermal noise method

The thermal noise method of determining the deflection sensitivity requires prior calibration of the cantilever spring constant and the ability to measure the thermal noise spectrum of the cantilever<sup>67</sup>. The thermal noise method is often integrated into modern AFM control software and can be used in tandem with the Sader method (see below) for quick analysis and calculation of both the spring constant and deflection sensitivity. However, it may be difficult or impossible to use the thermal noise method on stiffer ( $k > 10$  N/m) cantilevers due to decreased vibration amplitude. Additionally, the reported relative uncertainty of the thermal noise method is significantly larger,  $\sim 20\%$  compared to the hard surface contact method described above<sup>70</sup>. This technique cannot be used if the thermal tune method for determining the spring constant described below is being employed<sup>67</sup>.

### Spring constant

The gold standard for measuring cantilever spring constants is laser Doppler vibrometry (LDV), and there are now many commercially available probes that come with LDV-derived spring constant calibration information provided by the manufacturer for each individual probe (see **Table of Materials**). However, while accurate measurement of the cantilever spring constant is an absolute necessity for quantitative nanomechanical measurements, the practical methods for doing so in the typical laboratory for non-

calibrated probes are widely varied and can be somewhat complex. As such, only a brief overview of the two most common on-site spring constant calibration methods is provided here, with a listing of additional methods and appropriate literature citations to consult for more information.

### Thermal tune method

Likely the most common method available in today's commercial AFMs, the thermal tune method for determining cantilever spring constants is built into the control software for many systems. While not ideal for stiffer cantilevers ( $k > 10$  N/m) due to reduced cantilever deflection detection and limited electronics bandwidth, the thermal tune method is relatively easy to implement and is valid for a wide range of tip geometries<sup>71</sup>. The thermal tune method utilizes measurement and fitting of the cantilever's thermal noise spectrum, followed by application of the equipartition theorem to calculate the cantilever's potential energy, with the cantilever generally modeled as a simple harmonic oscillator<sup>72</sup>. The thermal tune method has an error of ~5%-10% for soft probes and is applicable for any cantilever shape<sup>73,74</sup>. For more detailed information, see the references cited in this section.

### Sader method

The Sader method is another method often integrated into the control software of many modern AFMs<sup>75,76,77</sup>. The Sader method uses the hydrodynamic load experienced by a cantilever as it vibrates in a fluid medium (usually air or water) along with the cantilever's plan view dimensions and quality factor to calculate the cantilever spring constant. The Sader method leads to an error of ~10%-15% for the cantilever spring constant<sup>74</sup>. Corresponding papers on the "original method"<sup>76,78</sup>, "general method"<sup>79</sup>, an extension of

the general method<sup>77</sup>, and instrument specific documentation can provide further details.

### Other methods

There are several other methods that have been developed and implemented to determine the spring constant of AFM cantilevers that are beyond the scope of this paper. Though none of these methods are as easy to implement or as widespread as the Sader or thermal tune calibration methods, they each possess unique advantages and disadvantages; the cited literature provides details regarding their application and implementation. In particular, Sikora provides an excellent review of many spring constant calibration methods and is an excellent resource on the topic<sup>72</sup>. A non-exhaustive list of other methods to determine spring constants includes laser Doppler vibrometry (LDV)<sup>73,74,80</sup>, micro-electrical-mechanical systems (MEMS) based devices<sup>81</sup>, reference cantilever<sup>82,83</sup>, added mass (both dynamic<sup>75</sup> and static<sup>84</sup>), precision balance<sup>85,86</sup>, electromagnetic actuation<sup>87</sup>, and finite element analysis (FEA)<sup>88,89</sup>.

### Tip radius

Common methods for determining the tip radius include both secondary electron SEM imaging and the blind tip reconstruction method (BTR).

### SEM analysis

Secondary electron SEM imaging can provide resolution down to 1 nm, enabling progressive images of wear to be directly and easily compared. A downside to SEM imaging is that because only highly experimental combined AFM-SEM tools exist<sup>90</sup>, the AFM probe must typically be unmounted and transported to the SEM for analysis, which can be both time-consuming and potentially subject the probe to

contamination. Another downside to SEM is that the resulting image is inherently a 2D projection of the tip, with no quantitative 3D information available. Care must be taken to align the probe in the exact same orientation each time for comparative results to be meaningful, as even small changes in the incident angle of the electron beam can alter the apparent size and shape of the probe tip. Finally, SEM imaging can be plagued by charging effects and carbon contamination, which may blur the image or cause physical changes to the probe tip, respectively.

### Blind tip reconstruction

In contrast to SEM, the BTR method is an *in situ* technique in which the 3D tip geometry is modeled based on imaging of a sample with numerous sharp (high aspect ratio) features much smaller than the radius of the probe. This method works because in AFM, the observed image is always a convolution of the probe tip shape and the sample feature shape, so by modeling extremely sharp features as infinitely sharp, the tip shape can be estimated. Unfortunately, in addition to the assumption of infinitely sharp spikes (i.e., surface features much smaller than the tip radius), the BTR technique can be influenced by imaging noise and scanning parameters, so comparative images should be obtained using very similar imaging parameters. Additionally, because multiple "images" of the tip are used to reconstruct its geometry, a direct one-to-one inverse calculation of the tip shape is impossible. Because of its nature, the BTR method is only practically able to inform the user of the upper bound of the tip shape<sup>63</sup>, and the act of imaging the probe to implement the BTR method may lead to tip wear (e.g., dulling or chipping of the probe tip).

### Relative calibration

Sometimes, a particular probe property cannot be readily and accurately measured. For example, the spring constant of stiffer cantilevers is difficult or impossible to measure with the thermal tune method because of bandwidth and deflection limitations<sup>91</sup>. As discussed above, other methods for determining the spring constant do exist, but because the thermal tune method is integrated into many modern AFMs, it is often implemented for simple daily use. Likewise, the deflection sensitivity must always be calibrated prior to experimentation for the conversion of laser movement on the PSD to the physical deflection of the probe cantilever. Practically speaking, however, measurement of the tip radius is the most time-consuming calibration step, and the one most likely to damage the probe tip. If it is not possible to directly measure the tip radius *via* SEM or BTR, then a relative calibration procedure may be utilized as an alternative for determining the effective tip radius, provided a standard reference sample with minimal surface roughness (ideally atomically flat) and a well-known modulus close to the expected experimental modulus is available. Examples of such ideal reference standards for relative calibration include muscovite mica<sup>17,92,93,94,95</sup> and HOPG<sup>96</sup>, but also serve to highlight the difficulty in identifying suitable reference standards for softer samples with moduli in the kPa to MPa range. To perform a relative calibration, first the deflection sensitivity should be calibrated as described in the main protocol. Second, the nominal spring constant for the probe should be inputted (usually supplied with the probe) or measured *via* one of the methods described above. The third step is indentation on the modulus reference standard sample surface using appropriate parameters. Finally, the collected F-D curve data should be analyzed and the tip radius parameter adjusted until the experimentally measured reduced modulus matches the expected reduced modulus. Note should be taken of the average deformation depth

achieved on the reference sample, as this depth **must be** maintained when indenting on the experimental sample of interest for the calibration to be relevant. Now, indentation on the sample of interest can occur, adjusting the ramp parameters to match the deformation depth achieved on the modulus standard reference material.

One advantage of the relative calibration method is that it avoids potential accumulated errors caused by inaccurate calibration of the deflection sensitivity, spring constant, and tip radius<sup>52</sup>. Additionally, it is perhaps slightly quicker and less likely to damage the probe than the BTR method. The biggest drawbacks to the relative calibration method are: 1) the need for a high quality reference sample with nm- to Angstrom-scale surface roughness and well-known mechanical properties similar to those of the sample of interest that can be analyzed with the same probe as the experimental sample, and 2) the requirement to achieve the same or very similar deformation depth on both the reference and experimental samples for the calibration to be valid. Accordingly, it is preferable to directly measure the tip radius if at all possible.

### Data analysis

The analysis method used to determine the mechanical properties of the sample from the measured F-D curves is just as important as the quality of the nanoindentation data itself. There are several common contact mechanic theories that model force-displacement relationships based on varying underlying assumptions (and hence, applicable in different scenarios). These contact mechanics models include Hertz<sup>97</sup>, Sneddon<sup>28</sup>, JKR (Johnson, Kendall, and Roberts)<sup>98</sup>, DMT (Derjaguin, Muller, and Toporov)<sup>35,99</sup>, MD (Maugis-Dugdale)<sup>100</sup>, and MYD (Muller, Yushchenko, and

Derjaguin)<sup>101,102</sup>. An in-depth analysis and comparison of various contact mechanics models and their application for analysis has been presented elsewhere<sup>29,30,103,104</sup>. While it is beyond the scope of this paper, **Table 4** provides a brief overview of some of the most common contact mechanics models. Of particular note, more complex models such as JKR, DMT, and others incorporate the effects of tip-sample adhesion<sup>30,35,98,99,100,101,102,103,104</sup>, which can be significant and is often easily identifiable by the appearance of negative deflection in the force curve (see **Figure 3**). In practice, the chosen analysis model is used to fit the collected F-D data and determine the mechanical properties, such as the elastic modulus. To properly fit the data, a flat baseline is necessary to determine the initial contact point or an effective contact point that fits the portion of the experimental data with the largest correlation to the model.



Theory	Applicability	Assumptions	Limitations
<b>Hertz</b>	Simple; often used for samples in fluid.	No adhesion.	Invalid for systems that have adhesive forces present.
<b>Derjaguin-Muller-Toporov (DMT)</b>	Stiff with small deformations.	Short-range adhesion in contact region plus long-range adhesion outside of contact region.	Restricted geometry may cause an underestimation of the contact area.
<b>Johnson-Kendall-Roberts (JKR)</b>	Soft with large deformations.	Short-range adhesive forces in the contact region only.	Can underestimate load due to adhesion.
<b>Maugis – Dugdale (MD)</b>	This general solution covers the other adhesive models.	Tip-sample interface modeled as a crack.	Analytical solution involving parametric equations.

**Table 4: Common contact mechanics models.** Selected common contact mechanics models with applicability, assumptions, and limitations noted.

The practical application of the models mentioned above for analyzing F-D curves requires the use of computer software to enable the large-scale batch processing of thousands or millions of curves in a short amount of time and perform statistical analysis on the results. In-house written code is often used in the analysis of F-D data, and various AFM manufacturers also provide software packages. However, due to its open-source nature, ease of use, and detailed supplementary information, the authors recommend the use of AtomicJ<sup>23</sup>. The program allows for simple and accurate analysis of F-D data using any of the theories described above as well as several others. Because the code is open source, it is easy to manipulate and customize for specific use-cases without the need to build complex code from scratch. Refer to Hermanowicz et al.<sup>23</sup> for in depth information on the AtomicJ software package.

In conclusion, through careful calibration of the probe, the contact area and force applied by an AFM probe tip to a sample surface can be quantified to enable determination of nanoscale mechanical properties, in particular the elastic modulus. A generalized protocol highlighting best practices to successfully implement AFM cantilever-based nanoindentation in air or fluid on both soft and hard samples, with elastic moduli ranging from kPa to GPa, has been presented with representative examples provided. Important considerations such as probe selection (including sample surface roughness, feature sizes, probe aspect ratio, and tip wear), probe calibration, and data analysis (including contact mechanics models and measurement statistics) have been discussed. Finally, co-localization of AFM-derived nanomechanical maps with other characterization techniques providing compositional information such as SEM/EDS has been demonstrated, as well as an example of measurement of a nanomechanical property other than elastic modulus (i.e., lipid bilayer rupture force) *via* AFM cantilever-based

nanoindentation to provide examples of additional synergistic applications of the technique. Taken together, the examples and discussion provided here should provide an entry point for researchers seeking to employ AFM cantilever-based nanoindentation to measure the mechanical properties of virtually any sample type.

## Disclosures

The authors have no conflicts of interest to disclose.

## Acknowledgments

All AFM experiments were performed in the Boise State University Surface Science Laboratory (SSL). SEM characterization was performed in the Boise State Center for Materials Characterization (BSCMC). Research reported in this publication regarding biofuel feedstocks was supported in part by the US Department of Energy, Office of Energy Efficiency and Renewable Energy, Bioenergy Technologies Office as part of the Feedstock Conversion Interface Consortium (FCIC), and under DOE Idaho Operations Office Contract DE-AC07-051ID14517. Cell mechanics studies were supported by the National Institutes of Health (USA) under grants AG059923, AR075803, and P20GM109095, and by National Science Foundation (USA) grants 1929188 and 2025505. The model lipid bilayer systems work was supported by the National Institutes of Health (USA) under grant R01 EY030067. The authors thank Dr. Elton Graugnard for producing the composite image shown in **Figure 11**.

## References

1. Hart, E. W. Theory of the tensile test. *Acta Metallurgica*. **15** (2), 351-355 (1967).

- Fell, J. T., Newton, J. M. Determination of tablet strength by the diametral-compression test. *Journal of Pharmaceutical Sciences*. **59** (5), 688-691 (1970).
- Babiak, M., Gaff, M., Sikora, A., Hysek, Š. Modulus of elasticity in three- and four-point bending of wood. *Composite Structures*. **204**, 454-465 (2018).
- Song, S., Yovanovich, M. M. Relative contact pressure-Dependence on surface roughness and Vickers microhardness. *Journal of Thermophysics and Heat Transfer*. **2** (1), 43-47 (1988).
- Hays, C., Kendall, E. G. An analysis of Knoop microhardness. *Metallography*. **6** (4), 275-282 (1973).
- Hill, R., Storåkers, B., Zdunek, A. B. A theoretical study of the Brinell hardness test. *Proceedings of the Royal Society of London. A. Mathematical and Physical Sciences*. **423** (1865), 301-330 (1989).
- Oliver, W. C., Pharr, G. M. An improved technique for determining hardness and elastic modulus using load and displacement sensing indentation experiments. *Journal of Materials Research*. **7** (6), 1564-1583 (1992).
- Sakharova, N. A., Fernandes, J. V., Antunes, J. M., Oliveira, M. C. Comparison between Berkovich, Vickers and conical indentation tests: A three-dimensional numerical simulation study. *International Journal of Solids and Structures*. **46** (5), 1095-1104 (2009).
- Cohen, S. R., Kalfon-Cohen, E. Dynamic nanoindentation by instrumented nanoindentation and force microscopy: a comparative review. *Beilstein Journal of Nanotechnology*. **4** (1), 815-833 (2013).
- Saha, R., Nix, W. D. Effects of the substrate on the determination of thin film mechanical properties by nanoindentation. *Acta Materialia*. **50** (1), 23-38 (2002).

11. Tsui, T. Y., Pharr, G. M. Substrate effects on nanoindentation mechanical property measurement of soft films on hard substrates. *Journal of Materials Research*. **14** (1), 292-301 (1999).
12. Cao, G., Gao, H. Mechanical properties characterization of two-dimensional materials via nanoindentation experiments. *Progress in Materials Science*. **103**, 558-595 (2019).
13. Castellanos-Gomez, A., Singh, V., van der Zant, H. S. J., Steele, G. A. Mechanics of freely-suspended ultrathin layered materials. *Annalen der Physik*. **527** (1-2), 27-44 (2015).
14. Cao, C., Sun, Y., Filleter, T. Characterizing mechanical behavior of atomically thin films: A review. *Journal of Materials Research*. **29** (3), 338-347 (2014).
15. Lee, C., Wei, X., Kysar, J. W., Hone, J. Measurement of the elastic properties and intrinsic strength of monolayer graphene. *Science*. **321** (5887), 385-388 (2008).
16. Elibol, K. et al. Visualising the strain distribution in suspended two-dimensional materials under local deformation. *Scientific Reports*. **6** (1), 28485 (2016).
17. Castellanos-Gomez, A. et al. Mechanical properties of freely suspended atomically thin dielectric layers of mica. *Nano Research*. **5** (8), 550-557 (2012).
18. Song, L. et al. Large scale growth and characterization of atomic hexagonal boron nitride layers. *Nano Letters*. **10** (8), 3209-3215 (2010).
19. Castellanos-Gomez, A. et al. Elastic properties of freely suspended MoS<sub>2</sub> nanosheets. *Advanced Materials*. **24** (6), 772-775 (2012).
20. D'Costa, N. P., Hoh, J. H. Calibration of optical lever sensitivity for atomic force microscopy. *Review of Scientific Instruments*. **66** (10), 5096-5097 (1995).
21. Wu, Y. et al. Evaluation of elastic modulus and hardness of crop stalks cell walls by nano-indentation. *Bioresource Technology*. **101** (8), 2867-2871 (2010).
22. Barns, S. et al. Investigation of red blood cell mechanical properties using AFM indentation and coarse-grained particle method. *BioMedical Engineering OnLine*. **16** (1), 140 (2017).
23. Hermanowicz, P., Sarna, M., Burda, K., Gabryś, H. AtomicJ: An open source software for analysis of force curves. *Review of Scientific Instruments*. **85** (6), 063703 (2014).
24. Broitman, E. Indentation hardness measurements at macro-, micro-, and nanoscale: a critical overview. *Tribology Letters*. **65** (1), 23 (2016).
25. Tiwari, A. *Nanomechanical Analysis of High Performance Materials*. Springer. Netherlands. (2015).
26. Aggarwal, R. L., Ramdas, A. K. *Physical Properties of Diamond and Sapphire*. CRC Press. (2019).
27. Boyd, E. J., Uttamchandani, D. Measurement of the anisotropy of Young's modulus in single-crystal silicon. *Journal of Microelectromechanical Systems*. **21** (1), 243-249 (2012).
28. Harding, J. W., Sneddon, I. N. The elastic stresses produced by the indentation of the plane surface of a semi-infinite elastic solid by a rigid punch. *Mathematical Proceedings of the Cambridge Philosophical Society*. **41** (1), 16-26 (2008).
29. Lin, D. C., Dimitriadis, E. K., Horkay, F. Robust strategies for automated AFM force curve analysis-I. Non-adhesive

- indentation of soft, inhomogeneous materials. *Journal of Biomechanical Engineering*. **129** (3), 430-440 (2006).
30. Lin, D. C., Dimitriadis, E. K., Horkay, F. Robust strategies for automated AFM force curve analysis-II: Adhesion-influenced indentation of soft, elastic materials. *Journal of Biomechanical Engineering*. **129** (6), 904-912 (2007).
31. Haile, S., Palmer, M., Otey, A. Potential of loblolly pine: switchgrass alley cropping for provision of biofuel feedstock. *Agroforestry Systems*. **90** (5), 763-771 (2016).
32. Lu, X. et al. Biomass logistics analysis for large scale biofuel production: Case study of loblolly pine and switchgrass. *Bioresource Technology*. **183**, 1-9 (2015).
33. Susaeta, A., Lal, P., Alavalapati, J., Mercer, E., Carter, D. Economics of intercropping loblolly pine and switchgrass for bioenergy markets in the southeastern United States. *Agroforestry Systems*. **86** (2), 287-298 (2012).
34. Garcia, R. Nanomechanical mapping of soft materials with the atomic force microscope: methods, theory and applications. *Chemical Society Reviews*. **49** (16), 5850-5884 (2020).
35. Derjaguin, B. V., Muller, V. M., Toporov, Y. P. Effect of contact deformations on the adhesion of particles. *Journal of Colloid and Interface Science*. **53** (2), 314-326 (1975).
36. Ciesielski, P. N. et al. Engineering plant cell walls: tuning lignin monomer composition for deconstructable biofuel feedstocks or resilient biomaterials. *Green Chemistry*. **16** (5), 2627-2635 (2014).
37. Liu, K., Ostadhassan, M., Zhou, J., Gentzis, T., Rezaee, R. Nanoscale pore structure characterization of the Bakken shale in the USA. *Fuel*. **209**, 567-578 (2017).
38. Maryon, O. O. et al. Co-localizing Kelvin probe force microscopy with other microscopies and spectroscopies: selected applications in corrosion characterization of alloys. *JoVE*. (184), e64102 (2022).
39. Eliyahu, M., Emmanuel, S., Day-Stirrat, R. J., Macaulay, C. I. Mechanical properties of organic matter in shales mapped at the nanometer scale. *Marine and Petroleum Geology*. **59**, 294-304 (2015).
40. Li, C. et al. Nanomechanical characterization of organic matter in the Bakken formation by microscopy-based method. *Marine and Petroleum Geology*. **96**, 128-138 (2018).
41. Bouzid, T. et al. The LINC complex, mechanotransduction, and mesenchymal stem cell function and fate. *Journal of Biological Engineering*. **13** (1), 68 (2019).
42. Dupont, S. et al. Role of YAP/TAZ in mechanotransduction. *Nature*. **474** (7350), 179-183 (2011).
43. Wang, S. et al. CCM3 is a gatekeeper in focal adhesions regulating mechanotransduction and YAP/TAZ signalling. *Nature Cell Biology*. **23** (7), 758-770 (2021).
44. Sen, B. et al. Mechanical strain inhibits adipogenesis in mesenchymal stem cells by stimulating a durable  $\beta$ -catenin signal. *Endocrinology*. **149** (12), 6065-6075 (2008).
45. Sen, B. et al. mTORC2 regulates mechanically induced cytoskeletal reorganization and lineage selection in marrow-derived mesenchymal stem cells. *Journal of Bone and Mineral Research*. **29** (1), 78-89 (2014).

46. Sen, B. et al. Mechanically induced nuclear shuttling of  $\beta$ -catenin requires co-transfer of actin. *Stem Cells*. **40** (4), 423-434 (2022).
47. Newberg, J. et al. Isolated nuclei stiffen in response to low intensity vibration. *Journal of Biomechanics*. **111**, 110012 (2020).
48. Ding, Y., Xu, G.-K., Wang, G.-F. On the determination of elastic moduli of cells by AFM based indentation. *Scientific Reports*. **7** (1), 45575 (2017).
49. Khadka, N. K., Timsina, R., Rowe, E., O'Dell, M., Mainali, L. Mechanical properties of the high cholesterol-containing membrane: An AFM study. *Biochimica et Biophysica Acta. Biomembranes*. **1863** (8), 183625 (2021).
50. Castellana, E. T., Cremer, P. S. Solid supported lipid bilayers: From biophysical studies to sensor design. *Surface Science Reports*. **61** (10), 429-444 (2006).
51. Qian, L., Zhao, H. Nanoindentation of soft biological materials. *Micromachines*. **9** (12), 654 (2018).
52. Pittenger, B., Yablon, D. Improving the accuracy of nanomechanical measurements with force-curve-based AFM techniques. *Bruker Application Notes*. **149** (2017).
53. Vorselen, D., Kooreman, E. S., Wuite, G. J. L., Roos, W. H. Controlled tip wear on high roughness surfaces yields gradual broadening and rounding of cantilever tips. *Scientific Reports*. **6** (1), 36972 (2016).
54. Bhaskaran, H. et al. Ultralow nanoscale wear through atom-by-atom attrition in silicon-containing diamond-like carbon. *Nature Nanotechnology*. **5** (3), 181-185 (2010).
55. Giannazzo, F., Schilirò, E., Greco, G., Roccaforte, F. Conductive atomic force microscopy of semiconducting transition metal dichalcogenides and heterostructures. *Nanomaterials*. **10** (4), 803 (2020).
56. Melitz, W., Shen, J., Kummel, A. C., Lee, S. Kelvin probe force microscopy and its application. *Surface Science Reports*. **66** (1), 1-27 (2011).
57. Kazakova, O. et al. Frontiers of magnetic force microscopy. *Journal of Applied Physics*. **125** (6), 060901 (2019).
58. Kim, H.-J., Yoo, S.-S., Kim, D.-E. Nano-scale wear: A review. *International Journal of Precision Engineering and Manufacturing*. **13** (9), 1709-1718 (2012).
59. Heath, G. R. et al. Localization atomic force microscopy. *Nature*. **594** (7863), 385-390 (2021).
60. Strahlendorff, T., Dai, G., Bergmann, D., Tutsch, R. Tip wear and tip breakage in high-speed atomic force microscopes. *Ultramicroscopy*. **201**, 28-37 (2019).
61. Lantz, M. A. et al. Wear-resistant nanoscale silicon carbide tips for scanning probe applications. *Advanced Functional Materials*. **22** (8), 1639-1645 (2012).
62. Khurshudov, A. G., Kato, K., Koide, H. Wear of the AFM diamond tip sliding against silicon. *Wear*. **203**, 22-27 (1997).
63. Villarrubia, J. S. Algorithms for scanned probe microscope image simulation, surface reconstruction, and tip estimation. *Journal of Research of the National Institute of Standards and Technology*. **102** (4), 425 (1997).
64. Kain, L. et al. Calibration of colloidal probes with atomic force microscopy for micromechanical assessment. *Journal of the Mechanical Behavior of Biomedical Materials*. **85**, 225-236 (2018).

65. Slattery, A. D., Blanch, A. J., Quinton, J. S., Gibson, C. T. Accurate measurement of Atomic Force Microscope cantilever deflection excluding tip-surface contact with application to force calibration. *Ultramicroscopy*. **131**, 46-55 (2013).
66. Dobrovinskaya, E. R., Lytvynov, L. A., Pishchik, V. *Sapphire: Material, Manufacturing, Applications*. Springer. US. (2009).
67. te Riet, J. et al. Interlaboratory round robin on cantilever calibration for AFM force spectroscopy. *Ultramicroscopy*. **111** (12), 1659-1669 (2011).
68. Pratt, J. R., Shaw, G. A., Kumanchik, L., Burnham, N. A. Quantitative assessment of sample stiffness and sliding friction from force curves in atomic force microscopy. *Journal of Applied Physics*. **107** (4), 044305 (2010).
69. Slattery, A. D., Blanch, A. J., Quinton, J. S., Gibson, C. T. Calibration of atomic force microscope cantilevers using standard and inverted static methods assisted by FIB-milled spatial markers. *Nanotechnology*. **24** (1), 015710 (2012).
70. Higgins, M. J. et al. Noninvasive determination of optical lever sensitivity in atomic force microscopy. *Review of Scientific Instruments*. **77** (1), 013701 (2006).
71. Lévy, R., Maaloum, M. Measuring the spring constant of atomic force microscope cantilevers: thermal fluctuations and other methods. *Nanotechnology*. **13** (1), 33-37 (2001).
72. Sikora, A. Quantitative normal force measurements by means of atomic force microscopy towards the accurate and easy spring constant determination. *Nanoscience and Nanometrology*. **2** (1), 8-29 (2016).
73. Ohler, B. Cantilever spring constant calibration using laser Doppler vibrometry. *Review of Scientific Instruments*. **78** (6), 063701 (2007).
74. Gates, R. S., Pratt, J. R. Accurate and precise calibration of AFM cantilever spring constants using laser Doppler vibrometry. *Nanotechnology*. **23** (37), 375702 (2012).
75. Cleveland, J. P., Manne, S., Bocek, D., Hansma, P. K. A nondestructive method for determining the spring constant of cantilevers for scanning force microscopy. *Review of Scientific Instruments*. **64** (2), 403-405 (1993).
76. Sader, J. E., Chon, J. W. M., Mulvaney, P. Calibration of rectangular atomic force microscope cantilevers. *Review of Scientific Instruments*. **70** (10), 3967-3969 (1999).
77. Sader, J. E. et al. Spring constant calibration of atomic force microscope cantilevers of arbitrary shape. *Review of Scientific Instruments*. **83** (10), 103705 (2012).
78. Sader, J. E. Frequency response of cantilever beams immersed in viscous fluids with applications to the atomic force microscope. *Journal of Applied Physics*. **84** (1), 64-76 (1998).
79. Sader, J. E., Pacifico, J., Green, C. P., Mulvaney, P. General scaling law for stiffness measurement of small bodies with applications to the atomic force microscope. *Journal of Applied Physics*. **97** (12), 124903 (2005).
80. Mendels, D.-A. et al. Dynamic properties of AFM cantilevers and the calibration of their spring constants. *Journal of Micromechanics and Microengineering*. **16** (8), 1720-1733 (2006).
81. Gao, S., Brand, U. In-situ nondestructive characterization of the normal spring constant of AFM cantilevers. *Measurement Science and Technology*. **25** (4), 044014 (2014).

82. Gibson, C. T., Watson, G. S., Myhra, S. Determination of the spring constants of probes for force microscopy/spectroscopy. *Nanotechnology*. **7** (3), 259-262 (1996).
83. Gates, R. S., Pratt, J. R. Prototype cantilevers for SI-traceable nanonewton force calibration. *Measurement Science and Technology*. **17** (10), 2852-2860 (2006).
84. Neumeister, J. M., Ducker, W. A. Lateral, normal, and longitudinal spring constants of atomic force microscopy cantilevers. *Review of Scientific Instruments*. **65** (8), 2527-2531 (1994).
85. Kim, M. S., Choi, I. M., Park, Y. K., Kang, D. I. Atomic force microscope probe calibration by use of a commercial precision balance. *Measurement*. **40** (7), 741-745 (2007).
86. Kim, M.-S., Choi, J.-H., Park, Y.-K., Kim, J.-H. Atomic force microscope cantilever calibration device for quantified force metrology at micro- or nano-scale regime: the nano force calibrator (NFC). *Metrologia*. **43** (5), 389-395 (2006).
87. Tian, Y. et al. A novel method and system for calibrating the spring constant of atomic force microscope cantilever based on electromagnetic actuation. *Review of Scientific Instruments*. **89** (12), 125119 (2018).
88. Clifford, C. A., Seah, M. P. The determination of atomic force microscope cantilever spring constants via dimensional methods for nanomechanical analysis. *Nanotechnology*. **16** (9), 1666-1680 (2005).
89. Chen, B.-Y., Yeh, M.-K., Tai, N.-H. Accuracy of the spring constant of atomic force microscopy cantilevers by finite element method. *Analytical Chemistry*. **79** (4), 1333-1338 (2007).
90. Mick, U., Eichhorn, V., Wortmann, T., Diederichs, C., Fatikow, S. Combined nanorobotic AFM/SEM system as novel toolbox for automated hybrid analysis and manipulation of nanoscale objects. *2010 IEEE International Conference on Robotics and Automation*. 4088-4093 (2010).
91. Kim, M.-S., Choi, J.-H., Kim, J.-H., Park, Y.-K. Accurate determination of spring constant of atomic force microscope cantilevers and comparison with other methods. *Measurement*. **43** (4), 520-26 (2010).
92. Zhang, G., Wei, Z., Ferrell, R. E. Elastic modulus and hardness of muscovite and rectorite determined by nanoindentation. *Applied Clay Science*. **43** (2), 271-281 (2009).
93. Bobko, C. P., Ortega, J. A., Ulm, F.-J. Comment on "Elastic modulus and hardness of muscovite and rectorite determined by nanoindentation" by G. Zhang, Z. Wei and R.E. Ferrell [Applied Clay Science 43 (2009) 271-281]. *Applied Clay Science*. **46** (4), 425-428 (2009).
94. Zhang, G., Wei, Z., Ferrell, R. E. Reply to the Comment on "Elastic modulus and hardness of muscovite and rectorite determined by nanoindentation" by G. Zhang, Z. Wei and R.E. Ferrell [Applied Clay Science 43 (2009) 271-281]. *Applied Clay Science*. **46** (4), 429-432 (2009).
95. Jin, D. W. et al. Thermal stability and Young's modulus of mechanically exfoliated flexible mica. *Current Applied Physics*. **18** (12), 1486-1491 (2018).
96. Xiao, J. et al. Anisotropic friction behaviour of highly oriented pyrolytic graphite. *Carbon*. **65**, 53-62 (2013).
97. Hertz, H. Ueber die Berührung fester elastischer Körper. *Journal für die reine und angewandte Mathematik*. **1882** (92), 156-171, (1882).

98. Johnson, K. L., Kendall, K., Roberts, A. D., Tabor, D. Surface energy and the contact of elastic solids. *Proceedings of the Royal Society of London. A. Mathematical and Physical Sciences*. **324** (1558), 301-313 (1971).
99. Muller, V. M., Derjaguin, B. V., Toporov, Y. P. On two methods of calculation of the force of sticking of an elastic sphere to a rigid plane. *Colloids and Surfaces*. **7** (3), 251-259 (1983).
100. Maugis, D. Adhesion of spheres: The JKR-DMT transition using a dugdale model. *Journal of Colloid and Interface Science*. **150** (1), 243-269 (1992).
101. Muller, V. M., Yushchenko, V. S., Derjaguin, B. V. On the influence of molecular forces on the deformation of an elastic sphere and its sticking to a rigid plane. *Journal of Colloid and Interface Science*. **77** (1), 91-101 (1980).
102. Muller, V. M., Yushchenko, V. S., Derjaguin, B. V. General theoretical consideration of the influence of surface forces on contact deformations and the reciprocal adhesion of elastic spherical particles. *Journal of Colloid and Interface Science*. **92** (1), 92-101 (1983).
103. Johnson, K. L., Greenwood, J. A. An adhesion map for the contact of elastic spheres. *Journal of Colloid and Interface Science*. **192** (2), 326-333 (1997).
104. Shi, X., Zhao, Y.-P. Comparison of various adhesion contact theories and the influence of dimensionless load parameter. *Journal of Adhesion Science and Technology*. **18** (1), 55-68 (2004).